

MACE-OFF: Short Range Transferable Machine Learning Force Fields for Organic Molecules

Dávid Péter Kovács^{*},¹ J. Harry Moore^{*},^{1,2} Nicholas J. Browning,³ Ilyes Batatia,¹ Joshua T. Horton,⁴ Yixuan Pu,⁵ Venkat Kapil,^{6,5,7} William C. Witt,⁸ Ioan-Bogdan Magdău,⁴ Daniel J. Cole,⁴ and Gábor Csányi^{1,2}

¹*Engineering Laboratory, University of Cambridge, Cambridge, CB2 1PZ, UK*

²*Ångström AI, Palo Alto, California, USA*

³*Swiss National Supercomputing Centre (CSCS), 6900, Lugano, Switzerland*

⁴*School of Natural and Environmental Sciences,*

Newcastle University, Newcastle upon Tyne NE1 7RU, UK

⁵*Department of Physics and Astronomy, University College, London WC1E 6BT, UK*

⁶*Yusuf Hamied Department of Chemistry, University of Cambridge, Lensfield Road, Cambridge, CB2 1EW, UK*

⁷*Thomas Young Centre and London Centre for Nanotechnology, London WC1E 6BT, UK*

⁸*Department of Materials Science and Metallurgy, University of Cambridge,*

27 Charles Babbage Road, CB3 0FS, Cambridge, United Kingdom

(Dated: January 30, 2025)

Classical empirical force fields have dominated biomolecular simulation for over 50 years. Although widely used in drug discovery, crystal structure prediction, and biomolecular dynamics, they generally lack the accuracy and transferability required for first-principles predictive modeling. In this paper, we introduce MACE-OFF, a series of short range transferable force fields for organic molecules created using state-of-the-art machine learning technology and first-principles reference data computed with a high level of quantum mechanical theory. MACE-OFF demonstrates the remarkable capabilities of short range models by accurately predicting a wide variety of gas and condensed phase properties of molecular systems. It produces accurate, easy-to-converge dihedral torsion scans of unseen molecules, as well as reliable descriptions of molecular crystals and liquids, including quantum nuclear effects. We further demonstrate the capabilities of MACE-OFF by determining free energy surfaces in explicit solvent, as well as the folding dynamics of peptides. Finally, we simulate a fully solvated small protein, observing accurate secondary structure and vibrational spectrum. These developments enable first-principles simulations of molecular systems for the broader chemistry community at high accuracy and relatively low computational cost.

I. Introduction

Machine learning (ML) force fields have recently undergone major improvements in accuracy, robustness, and computational speed [1–13]. They are now routinely used in materials chemistry contexts where density functional theory was previously the method of choice. In these applications, available empirical force fields, such as the embedded-atom method [14], do not provide sufficient accuracy and transferability to describe many scientifically interesting and challenging phenomena. Successful applications of ML potentials include simulation of quenching of amorphous silicon [15], determination of the phase diagrams of inorganic perovskites [16] and alloys [17], and device-scale simulation of phase-change memory materials [18].

In contrast, simulating bio-organic systems entails a different set of trade-offs, with greater emphasis on simulating large systems over long timescales. This means that empirical force fields, which sacrifice accuracy for computational speed, continue to be used routinely to study molecular liquids, crystals, biological systems, and drug-like molecules [19–22].

Two alternatives to empirical force fields are available. The first is semi-empirical quantum mechanics,

such as the series of extended tight-binding models [23], which represents a low-cost solution for small molecules. The method is limited by its moderate accuracy compared to quantum chemistry methods, its restriction to modelling non-periodic systems (if not in principle, but in widely used implementations), and its cubic scaling with system size.

More recently, a number of transferable machine learning force fields have also been developed for organic chemistry. By “transferable”, here we mean that these potentials are capable of generalising in system size and both chemical and conformation space sufficiently well to perform stable molecular dynamics and accurate property prediction for a wide range of molecular systems beyond those on which the model was trained. The most notable are the series of ANI [24–27] and AIMNet potentials [8, 28, 29]. ANI potentials pioneered the use of local symmetry function-based feed-forward neural networks [30] trained on a large dataset of organic molecular geometries [31, 32] to create transferable ML force fields. The ANI-2x model became the most widely adopted ML force field and therefore serves as one of the primary points of comparison in this paper. The ANI-2x model was recently combined with a polarizable electrostatic model [33] in a hybrid ML/MM simulation setting, and also with a neural network based dispersion correction [34]. The AIMNet models apply a message passing architecture [35], where the initial em-

^{*} These authors contributed equally.

beddings are the ANI symmetry functions. They have also extended the applicability of the models to a larger set of chemical elements, as well as to charged species. These models relax the locality assumptions by incorporating electrostatic and dispersion interactions. The PhysNet model uses a message passing architecture [35] and in addition to the semi-local terms also includes long-range electrostatic and dispersion interactions [36].

Other recent bio-organic force fields include the FENNIX model, which combines a local equivariant machine learning model with a physical long-range functional form for electrostatics and dispersion [37]. The model was trained to reproduce the CCSD(T)/CBS energies of small molecules and molecular dimers. It was shown that FENNIX can be used to run stable dynamics of liquid water, solvated alanine dipeptides, and an entire protein in the gas phase. However, further benchmarking of this model is required to assess the accuracy of the intramolecular potential outside the training set and of condensed phase molecular dynamics simulations.

Similarly, the ANA2B potential employs a short-ranged ML potential, with long-ranged, classical multipolar electrostatics, polarization and dispersion interactions [38]. Although this long-ranged model shows promising accuracy for condensed phase properties and crystal structure ranking, its accuracy and computational performance has not yet been demonstrated for larger biomolecules.

The GEMS model [39], built on the SpookyNet architecture [40], is another recent ML force field for biomolecular simulations. Whilst a transferable version of this potential is capable of producing stable dynamics for challenging biomolecular systems, certain properties, for example the folding dynamics of small peptides, require the addition of system-specific training configurations in order to accurately reproduce experimental properties. More recently, the transferable SO3LR potential was introduced by the same group of researchers [41]. This is based on the equivariant SO3krates architecture and also includes analytic dispersion and electrostatic long range contributions. Whilst this potential is capable of fast and stable simulations of biomolecular systems, we are not yet aware of more extensive quantitative benchmarking on off-equilibrium energetics or thermodynamic properties.

In this paper, we introduce a family of five purely local (i.e. short range), transferable bio-organic machine learning force fields which we refer to collectively as MACE-OFF. The force fields are parameterized for the ten most important chemical elements for organic chemistry: H, C, N, O, F, P, S, Cl, Br, and I. They are capable of accurately describing intra- and intermolecular interactions of neutral closed-shell systems. This enables the simulation of a wide range of chemical systems, from molecular liquids and crystals to drug-like molecules and biopolymers.

The models were validated on a number of tasks, including the prediction of small molecule torsion barriers, geometry optimizations, calculations of lattice param-

eters and enthalpies of formation of molecular crystals, and the calculation of the Raman spectra of molecular crystals, including nuclear quantum effects. We have also validated the models for predicting the densities and heats of vaporization of a range of molecular liquids. In particular, we study how well MACE-OFF reproduces the fundamental properties of water, including density and radial distribution functions. To further showcase the capabilities of the model, we computed the free energy surface and J-coupling parameters of alanine tripeptide (Ala₃) in vacuum and explicit water, and simulated the folding of Ala₁₅ at different temperatures. We also carried out an all-atom simulation of the protein crambin in explicit water (18 000 atoms), where we observed the correct secondary structure motifs and computed its vibrational spectrum, finding good agreement with other ML potentials and previously reported experimental data. Finally, we tested the computational speed of the current implementation in the LAMMPS and OpenMM simulation packages, demonstrating both strong and weak scaling.

While truly general purpose force fields for biomolecular modeling do need to include formally long-range Coulomb interactions, the purpose of this paper is to push the capabilities of short-range potentials as far as they can go, in part as preparation for including explicit polarizable electrostatic interactions in the future.

II. Methods

A. The MACE architecture

The MACE model [2] is a force field that maps the positions and chemical elements of atoms to the system’s potential energy. Linear scaling with system size is achieved by decomposing the total energy into atomic site energies. First, a graph is defined by connecting two nodes (atoms) by an edge if they are in each other’s local environment. The local environment $\mathcal{N}(i)$ is the set of all atoms j around the central atom i for which $\|\mathbf{r}_{ij}\| \leq r_{\text{cut}}$, where \mathbf{r}_{ij} is the vector from atom i to atom j and r_{cut} is the cutoff hyperparameter. The array of features of node i is denoted by $\mathbf{h}_i^{(t)}$ and is expressed in the spherical harmonic basis, with its elements indexed by l and m . The superscript in t indicates the iteration steps (corresponding to “layers” of message passing in the language of graph neural networks). All MACE-OFF models are made up of two layers. The $\mathbf{h}_i^{(t)}$ features depend on the chemical environment of the atoms for $t > 0$.

The node features $\mathbf{h}_i^{(0)}$ are initialized as a (learnable) embedding of the chemical elements with atomic numbers z_i into k channels:

$$h_{i,k00}^{(0)} = \sum_z W_{kz} \delta_{zz_i} \quad (1)$$

The superscript (0) in this case indicates the initial (0-

th) layer. This type of mapping has been widely applied to graph neural networks [42–44] and other models [45, 46].

Next, for each atom, the features of its neighbours are combined with the interatomic displacement vectors, \mathbf{r}_{ij} , to form the one-particle basis $\phi_{ij,k\eta_1 l_3 m_3}^{(t)}$. The radial distance is used as an input into a learnable radial function $R(r_{ij})$ with several outputs that correspond to the different ways in which the displacement vector and the node features can be combined while preserving equivariance [47]:

$$\phi_{ij,k\eta_1 l_3 m_3}^{(t)} = \sum_{l_1 l_2 m_1 m_2} C_{\eta_1, l_1 m_1 l_2 m_2}^{l_3 m_3} R_{k\eta_1 l_1 l_2 l_3}^{(t)}(r_{ij}) \times Y_{l_1}^{m_1}(\hat{\mathbf{r}}_{ij}) h_{j,kl_2 m_2}^{(t)} \quad (2)$$

where Y_l^m are the spherical harmonics, and $C_{\eta_1, l_1 m_1 l_2 m_2}^{l_3 m_3}$ denotes the Clebsch-Gordan coefficients. There are multiple ways of constructing an equivariant combination with a given symmetry (l_3, m_3) , and these multiplicities are enumerated by the index η_1 [48].

The one-particle basis ϕ is summed over the neighborhood and the k channels are mixed together with learnable weights to form the permutation invariant atomic basis A_i :

$$A_{i,kl_3 m_3}^{(t)} = \sum_{\bar{k}, \eta_1} W_{k\bar{k}\eta_1 l_3}^{(t)} \sum_{j \in \mathcal{N}(i)} \phi_{ij,\bar{k}\eta_1 l_3 m_3}^{(t)} \quad (3)$$

Higher-order (many-body) symmetric features are created on each atom i by taking tensor products of the atomic basis, A_i , with itself ν times, resulting in the “product basis”. The product basis is then contracted with the generalized Clebsch-Gordan coefficients, $\mathcal{C}_{\eta_\nu, \mathbf{l}\mathbf{m}}^{LM}$, to obtain the equivariant many-body basis, \mathbf{B}_i [48],

$$\mathbf{B}_{i,\eta_\nu kLM}^{(t),\nu} = \sum_{\mathbf{l}\mathbf{m}} \mathcal{C}_{\eta_\nu, \mathbf{l}\mathbf{m}}^{LM} \prod_{\xi=1}^{\nu} A_{i,kl_\xi m_\xi}^{(t)} \quad (4)$$

where bold $\mathbf{l}\mathbf{m}$ denotes the ν -tuple of l and m values and similarly to Equation (2), η_ν enumerates the number of possible couplings to create the features with equivariance LM . The maximum body-order is controlled by the parameter ν and is fixed at 3 (corresponding to 4-body terms, which includes the central atom) for all MACE-OFF models in this work.

Finally, a “message” m_i is created on each atom as a learnable linear combination of the equivariant many-body features:

$$m_{i,kLM}^{(t)} = \sum_{\nu} \sum_{\eta_\nu} W_{z_i \eta_\nu kL}^{(t),\nu} \mathbf{B}_{i,\eta_\nu kLM}^{(t),\nu} \quad (5)$$

The recursive update of the node features ($t : 0 \rightarrow 2$) is obtained by adding the message to the atoms’ features from the previous iteration, with weights that depend on the chemical element (z_i):

$$h_{i,kLM}^{(t+1)} = \sum_{\bar{k}} W_{kL,\bar{k}}^{(t)} m_{i,\bar{k}LM}^{(t)} + \sum_{\bar{k}} W_{kz_i L,\bar{k}}^{(t)} h_{i,\bar{k}LM}^{(t)} \quad (6)$$

Since the initial node features $\mathbf{h}^{(0)}$ are only dependent on the chemical element of the atom, the second term of Eq. (6) is not included in the first layer. This makes it possible to set the energy of the isolated atoms (that is, those with no neighbours) exactly [49], which is often desirable [37, 50]. The MACE models in this work have an effective receptive field of $2 \times r_{\text{cut}}$ due to the two layers of message passing.

The site energy is a sum of read-out functions applied to node features from the first and second layers. The read-out function is defined as a linear combination of rotationally invariant node features for the first layer, and as multi-layer perceptron (MLP) for the second layer.

$$E_i = \sum_{t=1}^2 E_i^{(t)} = \sum_{t=1}^2 \mathcal{R}^{(t)}(\mathbf{h}_i^{(t)}), \quad (7)$$

$$\mathcal{R}^{(t)}(\mathbf{h}_i^{(t)}) = \begin{cases} \sum_k W_k^{(t)} h_{i,k00}^{(t)} & \text{for } t = 1 \\ \text{MLP}\left(\left\{h_{i,k00}^{(t)}\right\}_k\right) & \text{for } t = 2 \end{cases} \quad (8)$$

The forces and stresses on the atoms are calculated by taking analytical derivatives of the total potential energy with respect to the positions of the atoms and the components of the deformation tensor in the periodic setting, as is usual.

B. Training data

The core of the training set is version 1 of the SPICE dataset [51] with 95% of the data used for training and validation, and 5% set aside for testing. Test/train splitting was performed at the molecule level, ensuring conformers of the same molecule do not appear in both train/validation and test sets. Table I summarizes the training and test sets. The MACE-OFF models are trained to reproduce the energies and forces computed at the ω B97M-D3(BJ)/def2-TZVPPD level of quantum mechanics [52–56], as implemented in the PSI4 software package [57]. We have used a subset of SPICE that contains the ten chemical elements H, C, N, O, F, P, S, Cl, Br, and I, and has a neutral formal charge (see Table 2 in Ref. [51] for element coverage in the dataset). We have also removed the ion pairs subset. Overall, we used about 85% of the full SPICE dataset. The geometries in the SPICE dataset have been generated by running molecular dynamics simulations using classical force fields [58], performed at both 300K and 500K, and sampling maximally different conformations from the resulting trajectories [51].

The SPICE dataset only contains small molecules of up to 50 atoms. To facilitate the learning of intramolecular non-bonded interactions, we augmented SPICE with larger 50–90 atom molecules randomly selected from the QMugs dataset [60]. The geometries

Table I. **Summary of training and test sets.** The columns PubChem to Solvated Amino Acids correspond to the SPICE dataset [51].

	PubChem	DES370K Monomers	DES370K Dimers [59]	Dipeptides	Solvated Amino Acids	Water	QMugs [60]	Tripeptides
Chemical elements	H, C, N, O, F, P, S, Cl, Br, I	H, C, N, O, F, P, S, Cl, Br, I	H, C, N, O, F, P, S, Cl, Br, I	H, C, N, O, S	H, C, N, O, S	H, O	H, C, N, O, F, P, S, Cl, Br, I	H, C, N, O
System size	3-50	3-22	4-34	26-60	79-96	3-150	51-90	30-69
# Train	646821	16861	263065	19773	948	1597	2748	0
# Test	33884	889	13896	1025	52	84	144	898

were generated by running molecular dynamics simulations using GFN2-xTB [23] similarly to the protocol described in Ref. [61]. The energies and forces were re-evaluated at the level of QM theory used in SPICE. Finally, to obtain a better description of water, the dataset was further augmented with a number of water clusters carved out of molecular dynamics simulations of liquid water [62], with sizes of up to 50 water molecules. In addition to the 5% of each subset, part of the COMP6 tripeptide dataset [25] was also recomputed at the SPICE level of theory and used as part of the test evaluation, but not for training.

After fitting the small MACE model (see Section II C) and observing the training errors, we noticed the presence of outliers in the dataset. This is probably caused by errors in the underlying electronic structure calculations, some of which have been documented on the SPICE GitHub repository.* To confirm this, we also re-evaluated a selection of the configurations that had the highest error, using the level of DFT used in SPICE, and found that for about a third of the configurations, the recomputed energies and forces agreed well with the MACE prediction and not with the original DFT labels. To purify the dataset, we removed from the training set the configurations that had a maximum force error greater than 2 eV/Å. This meant the removal of just 808 configurations, many of which contained heavy elements, in particular phosphorus and iodine, that might have a more challenging electronic structure.

In order to understand the role additional data plays in the performance of the model, we also investigated the difference in performance due to inclusion of additional configurations released as part of the second version of SPICE [63]. The updated dataset, which we incorporate into the MACE-OFF24(M) model (see Section II C), contains among others, an additional 208,000 configurations comprising solvated PubChem molecules and amino acid-ligand pairs. The former were sampled from molecular dynamics using the same protocol as in the original dataset, whilst the amino acid-ligand pairs were extracted from structures in the PDB. This release

also contained 1000 water clusters, containing up to 90 atoms. These were also included and used to complement the set of water clusters we had already included in the extended dataset.

In common with the first version of SPICE, close inspection of this new set revealed several nonphysical geometries with correspondingly high DFT forces. These configurations were removed by applying a maximum force filter of 15 eV/Å. We also observed that many phosphorous-containing compounds were present among the outliers, as well as configurations with highly distorted geometries, which also suggest challenging electronic structure. We also found that many configurations had forces that do not sum to zero. To avoid the possibility of these configurations poisoning the dataset, we applied a total force filter of 0.1 eV/Å. In total this removed 10,372 configurations from the SPICE v2 subsets.

C. Model details

The MACE model has parameters that enable systematic control of model expressivity (and subsequent accuracy) against computational cost. In this paper, we present three variants of the MACE-OFF23 model, a small, a medium, and a large one, denoted in the text as MACE-OFF23(S), MACE-OFF23(M) and MACE-OFF23(L) respectively. The models get more accurate with size, but also have an increasing computational cost. The small model is well suited for large-scale simulations, the medium model offers a good balance of speed and accuracy, and the large model is best used for small systems or when the highest possible accuracy is desirable.

Table II. Hyperparameters of the MACE-OFF models

	23(S)	23(M)	23(M)b	23(L)	24(M)
Cutoff radius (Å)	4.5	5.0	6.0	5.0	6.0
Chemical channels	96	128	128	192	128
k (see Eq. (1))	96	128	128	192	128
max L (see Eq. (5))	0	1	1	2	1
SPICE version	1	1	1	1	2

* <https://github.com/openmm/spice-dataset>

The hyperparameters of the models are displayed in Table II. The MACE-OFF23(S) model has 96 channels, $L = 0$ invariant messages, and a cutoff of 4.5 Å. The MACE-OFF23(M) model has 128 channels and $L = 1$ messages, and the MACE-OFF23(L) has 192 channels and $L = 2$ equivariant messages. Medium and large models have a cutoff of 5.0 Å in each layer. In light of the additional configurations added to the SPICE dataset during this work, we present two additional models that improve upon the performance of the original three MACE-OFF23 models. MACE-OFF23(M)b is identical to the medium model except for the increased 6 Å cutoff, which we find is crucial for recovering certain properties of condensed phase systems. MACE-OFF24(M) retains the extended 6 Å cutoff and includes additional configurations from SPICE v2 dataset [63]. MACE-OFF23(M)b can therefore be viewed as an ablation of the MACE-OFF24(M) model, enabling insight into which properties are driven by the extended cutoff and those that additionally require the additional non-bonded interaction datasets. All models were trained using the PyTorch [64] implementation of MACE, available on <https://github.com/ACESuit/mace>. For more information about the training, please refer to the SI.

D. MACE-OFF23- μ

In addition to the series of MACE-OFF force field models, we also present MACE-OFF23- μ , which predicts the total dipole moment of molecules and can be used to estimate vibrational spectra based on the autocorrelation of the dipole moment. The model architecture is identical to the MACE architecture described above, with the only difference being the readout function, which produces an $L = 1$ tensor for each atom instead of the atomic site energies. Given the equivariant order of the readout, the smallest possible model corresponds to the ‘medium’ architecture, which is the one considered in this work. Other than the readout’s equivariant order, all hyperparameters match those of the MACE-OFF23(M) model. MACE-OFF23- μ was trained on the subset of SPICE v1 for which a total dipole moment was available, resulting in the exclusion of the QMugs and water subsets.

III. Results

A. Extended SPICE Test Set

First, we look at the pointwise errors of the energy and force predictions on a held-out test set for each of the three baseline MACE-OFF23 models. Figure 1 shows the per-atom energy, force and intermolecular force root-mean-square errors (full statistics are provided in SI Table IV). As the size of the model

increases, the models gradually become more accurate, with the large model generally achieving errors of around 0.5–1.0 meV/atom and 15–20 meV/Å, well below the 1 kcal/mol (43 meV) chemical accuracy limit for the drug-like organic molecules studied here.

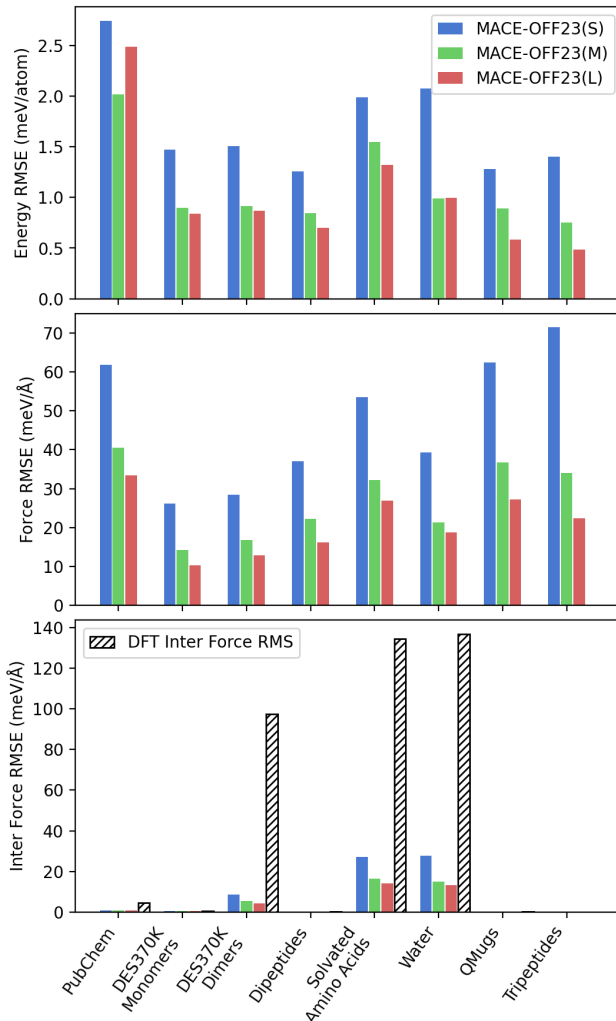


Figure 1. **Test set root mean square errors (RMSE).** Errors in the MACE-OFF23 models compared to the underlying DFT reference data, highlighting the relative accuracy of the three models. Bottom panels show specifically inter-molecular force errors compared to overall DFT inter-molecular force magnitudes (RMS) and note the absence of results for subsets that are composed of single molecules (i.e. DES370K Monomers, Dipeptides, QMugs, Tripeptides). Note that for subsets comprising only single molecule configurations (i.e. DES370K Monomers, Dipeptides, QMugs, Tripeptides) inter-molecular contributions are expected to be zero. The slight deviation from zero arises because DFT forces do not obey translational and rotational symmetries with sufficient accuracy, while MACE models do (check SI section B for details).

The last column represents an extrapolation task, the training set contains only dipeptides, and this test set looks at tripeptides, indicating that the models are able

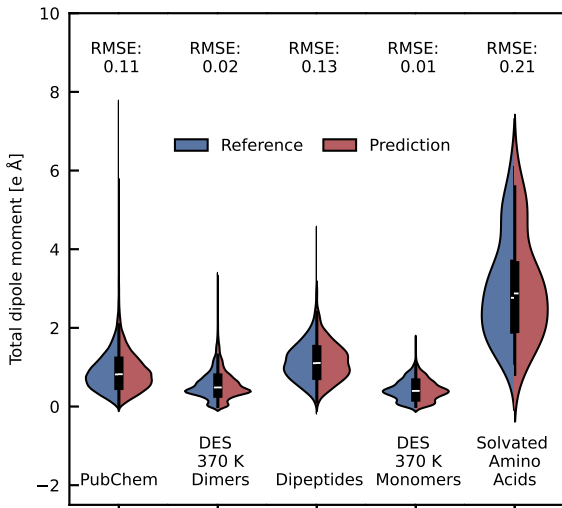


Figure 2. **Test set prediction and root mean square errors (RMSE).** Violin plots of the reference (blue) and predicted (red) distributions of the dipole moment predicted using MACE-OFF23- μ . The RMSEs are reported above the violin plots for the individual test sets.

to extrapolate to larger fragments with more complex interactions, with no loss of accuracy.

The bottom panel of Figure 1 shows specifically the intermolecular force errors, which were obtained by separating the force contributions to molecular translations and rotations (see SI and Ref. [65] for details). These interactions are crucial as they underpin the thermodynamics and transport properties in the organic condensed phase. MACE-OFF23(M) and MACE-OFF23(L) both yield similar errors of around 5–15 meV/Å, which are about 1.5–3 times smaller than total force errors, and about 5–10% of the typical DFT intermolecular force magnitude (RMS). For context, relative intramolecular force errors, which are roughly equivalent to total force errors, are around 1–2%. The latter are routinely used across the literature to benchmark ML models, however, we advocate that intermolecular RMSE errors are a more appropriate metric to assess model accuracy for organic condensed phase applications. The results here demonstrate the remarkable accuracy of MACE models in predicting these subtle but crucial interactions. We will investigate how these energy and force errors translate into condensed phase physical property predictions in later Sections.

We also assess the accuracy of the MACE-OFF23- μ model on the test sets, evaluating its effectiveness for predicting dipole moments and infrared spectra of organic molecules. Figure 2 summarizes this performance by examining the alignment between the violin distributions of the reference and predicted total dipole moment

values, as well as the RMSEs. The small RMSEs and strong alignment of the distributions indicate high fidelity across the test datasets for which reference dipole moment values were available. These results suggest promising performance for zero-shot predictions of the dipole moments (and infrared spectra) of unseen organic molecules, as demonstrated in a recent benchmark on out-of-distribution drug-like molecules from the NIST database [66].

B. Dihedral scans

Next, we evaluate the performance of the MACE-OFF23 models on dihedral scans of drug-like molecules. This task is routinely carried out using quantum mechanical methods to create reference data for parameterizing classical empirical force field dihedral terms [67]. The task is particularly challenging, as constrained geometry optimizations can be difficult to converge if the potential energy surface is not smooth, as has been observed for example for the ANI-1x potential [68].

1. TorsionNet-500

The top panel of Figure 3 summarizes the results for the TorsionNet-500 dataset [70]. This dataset contains torsion drives of 500 different molecules, selected to cover a wide range of pharmaceutically relevant chemical space. The original data set was reported at the B3LYP/6-31G(d) level of DFT theory. For consistency with the SPICE dataset, we recreated the torsion profiles using the DFT setting of SPICE, which uses a higher level of theory and basis set (SI Section C).

The first panel shows an example of a torsion drive, indicating the complex energy profile that the MACE models are able to capture closely, including geometries far from equilibrium. The center panel shows the mean barrier height error of a number of representative models, comparing the Sage classical empirical force field [21], a semi-empirical quantum mechanical method GFN2-xTB [23], a recent transferable machine learning force field AIMNet2 [8], and the three MACE-OFF23 models. Again, systematic improvements in accuracy with MACE model size are observed, with medium and large models, in particular, achieving errors of around 0.25 kcal/mol compared to the reference method. The AIMNet2 model achieves comparable accuracy to the small MACE-OFF23 model. A similar conclusion can be drawn from the comparison of the molecular geometries by looking at the root mean squared deviation of the atomic positions averaged over the full torsion scans, as indicated by the top right panel of Figure 3. It shows that MACE-optimized geometries have a deviation of about 0.025 Å, meaning they are almost indistinguishable from DFT-optimized structures. It is important to

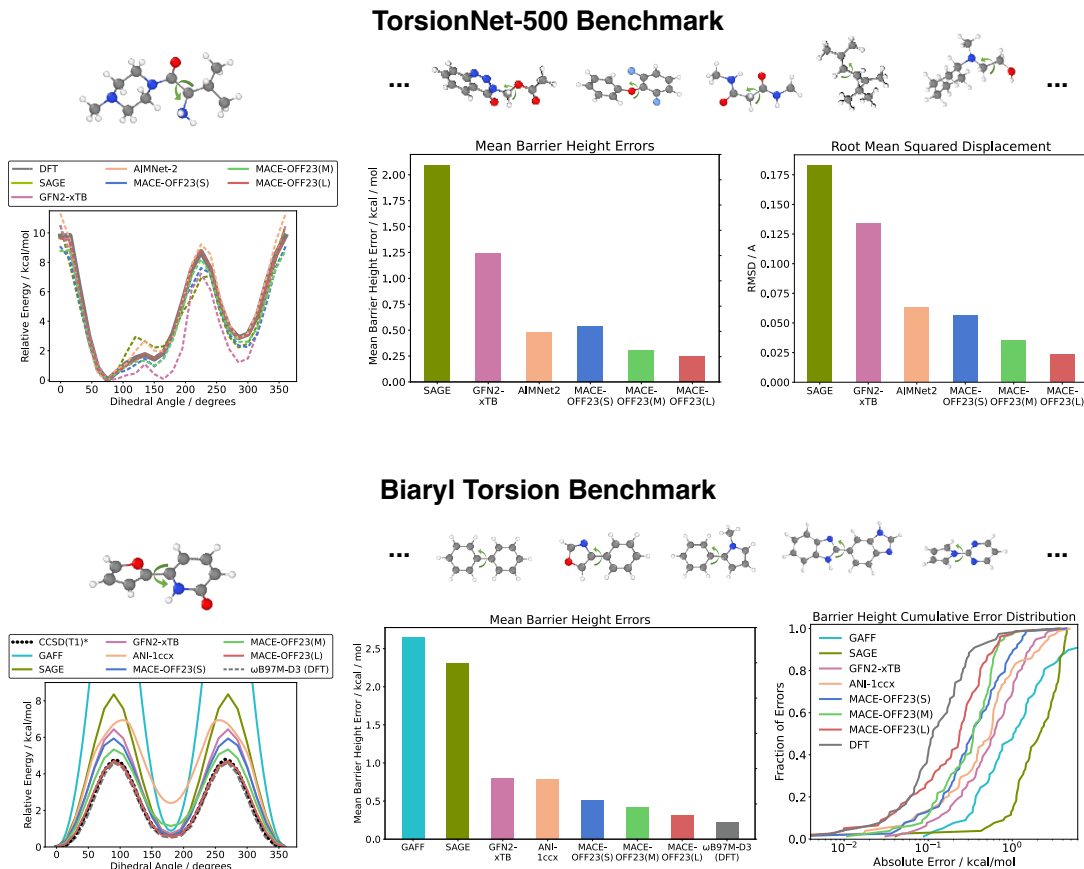


Figure 3. **Dihedral benchmark scans.** The top panel shows torsion drive data for the TorsionNet-500 dataset, which has a wide chemical diversity (five example molecules are shown). The bottom panel focuses on the torsion angle between two aromatic rings in the biaryl torsion benchmark [69] which contains 78 molecules (five examples are shown).

note that the other models were trained to different levels of DFT, which might also contribute to the observed differences.

2. Biaryl fragments

The biaryl torsion benchmark investigates the torsional profiles of about 100 different biaryl fragments computed at the coupled cluster level of theory [69]. In these molecules, the rotatable bond is between two aromatic rings. Such chemistry frequently occurs in drug-like molecules, and the profiles are typically challenging to model accurately using empirical classical force fields. Following previous studies, we used a subset of 78 molecules to facilitate comparisons with the ANI-1ccx model, which is only parameterized for H, C, N, and O chemical elements [69].

In the bottom panel of Figure 3, we compare the results of torsion drives of empirical force fields, semi-

empirical QM methods, and the ANI-1ccx machine learning force field [26] with the MACE-OFF23 models. We also compare the DFT potential energy surfaces (using the SPICE level of theory) with the published gold standard coupled cluster data.

The DFT torsion drives achieve a mean barrier height error of 0.2 kcal/mol with respect to coupled cluster data, and is therefore the best result theoretically possible for MACE-OFF23 models which were trained on the same DFT level of theory. We find that the large model comes close to this, with a mean absolute error of 0.3 kcal/mol. The medium and small MACE models have barrier height errors of 0.4 and 0.5 kcal/mol, respectively. Remarkably, the small MACE model is significantly more accurate than the next-best non-DFT methods, ANI-1ccx and GFN2-xTB, as illustrated in the bottom-center plot of Figure 3. In particular, unlike MACE-OFF23, coupled cluster reference calculations were used to parameterize the ANI-1ccx and GFN2 models. In the bottom right, we also show the cumula-

tive error distributions to verify that the MACE-OFF23 barrier height errors are not only accurate on average but are also robust, with essentially no outliers.

3. Infrared spectroscopy of a drug molecule

To assess the accuracy of the MACE-OFF23 and MACE-OFF23- μ models for finite temperature properties of molecules, we study the infrared spectrum of an isolated paracetamol molecule at room temperature. This is a stringent test, as reproducing the line positions and their relative intensities requires an accurate treatment of both intramolecular interactions and the dipole moment in out-of-equilibrium configurations. As shown in Figure 4, we estimate the classical and approximate quantum IR spectra [71] using the MACE-OFF23(M) and MACE-OFF23- μ models, and compare them directly with experimental data at 293 K [72]. For low and intermediate frequencies (up to around 2000 cm^{-1}), the classical and quantum spectra agree with each other and with the experimental data, allowing identification of all collective modes. For the high-frequency O-H and N-H modes, we observe that the classical spectra are shifted to the blue due to the absence of anharmonic zero-point fluctuations, which typically soften these bonds. A quantum treatment of nuclear dynamics results in good agreement with the experimental data, with the exception of a net blue shift, likely due to the limitations of the reference density functional. We also note a slight discrepancy in the relative intensities of the high-frequency stretching with respect to the lower-frequency modes. This could result from a limitation of the reference density functional or the MACE-OFF23- μ model, which we aim to investigate in a future study.

C. Molecular crystals

In the following, we demonstrate the ability of the MACE-OFF force fields to simulate the vibrational and thermal properties of molecular crystals.

1. Vibrational spectroscopy of paracetamol

Raman spectroscopy is one of the most widely used techniques for characterizing molecular crystals. Unlike IR spectroscopy, which only detects vibrational modes that distort dipoles, Raman spectroscopy is more sensitive to collective modes governed by weak, non-bonded interactions in a broad range of molecular materials. The low-frequency region of the Raman spectrum (e.g., the THz regime) gives a vibrational fingerprint of the intermolecular interactions. Thus, it is widely used to differentiate between polymorphs of molecular crystals. Meanwhile, the high-frequency Raman spectrum probes intramolecular modes and

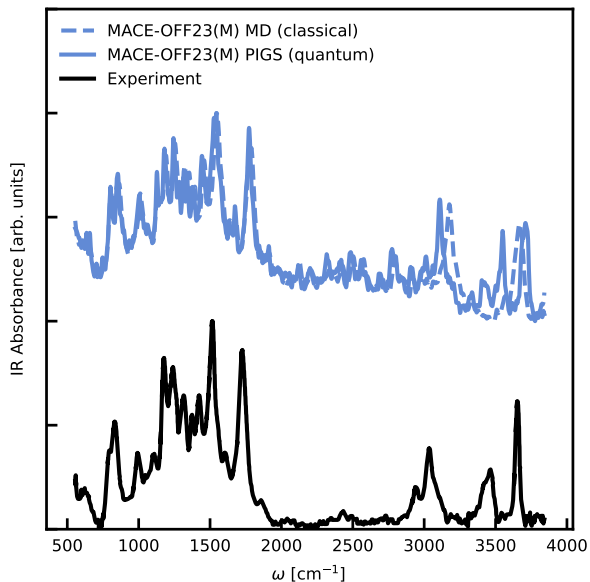


Figure 4. **Infrared (IR) spectrum of paracetamol molecule.** The classical (blue dashed) and quantum (blue solid) IR spectrum at 293 K using the MACE-OFF23(M) and MACE-OFF23- μ models by propagating the system and estimating the time correlation function of the time derivative of the total dipole moment. Quantum nuclear effects are incorporated using path-integral coarse-grained simulations (PIGS) [71]. The experimental data are taken from Ref. 72.

their coupling to low-frequency modes.

Here, we test the ability of the MACE-OFF23(S) model to predict the Raman spectrum of the “Form II” polymorph of paracetamol. To compare MACE-OFF23(S) directly with experiments, we rigorously incorporate quantum nuclear and non-Condon effects using our ML-aided framework [73]. We incorporate quantum nuclear effects by fitting an effective potential energy surface [71] (using MACE) to calculate quantum nuclear corrections to the MACE-OFF23(S) model within the path-integral coarse-grained simulations (PIGS) method. To incorporate non-Condon effects, we fit a separate equivariant MACE model to the first-principles polarizability of paracetamol polymorphs (data taken from Refs. 74, 75). The remaining steps of our quantum nuclear simulations mimic an entirely classical calculation involving a NVE molecular dynamics simulation, prediction of the isotropic and anisotropic components of the polarizability tensor, and calculation of their time correlation functions. For further details we refer the reader to Ref. 73.

As shown in Figure 5, we predict both the high- and low-frequency regions of the Raman spectrum of paracetamol form II with an overall good agreement with the experimental band positions [76]. Since the experiment captures the Raman spectra along different

crystal directions while we estimate the “powder” Raman spectrum [75], we do not compare band intensities. We find that the classical predictions (based on MACE classical MD) are consistently shifted with respect to the experiment. At the same time, quantum nuclear predictions (encoded by the PIGS method) play an essential role in improving the agreement between theory and experiments. Moreover, we note that a broad band at around 3300 cm^{-1} is only captured at the level incorporating quantum nuclear effects. The low-frequency modes also agree semi-quantitatively with the experiments and do not require a quantum nuclear description. The 2–3 % overall shift in the vibrational frequencies notwithstanding, the MACE-OFF23(S) combined with quantum nuclear effects and non-Condon effects shows promising capabilities for the characterization of molecular crystals.

2. Lattice enthalpies

Next, we assess the ability of the MACE-OFF23 force fields to describe the stability of molecular crystals. We computed the enthalpies of sublimation of a range of 23 representative small molecular crystals [78] following the protocol of Ref. [79].

Figure 6 compares the predicted sublimation enthalpies with the experimentally measured ones. This task is often used to test various DFT functionals. Since the ω B97M-D3(BJ) functional used to parameterize MACE-OFF23 does not have a periodic implementation, an estimate of the highest achievable accuracy is not available. The figure shows that the three MACE models are able to capture trends and improve significantly compared to the ANI-2x model. The large MACE-OFF23 model achieves a mean absolute error of just 1.7 kcal/mol, which is comparable to the errors of several different dispersion-corrected density functionals for a fraction of the computational cost [78].

We have also compared the relaxed unit cell vectors of the MACE-OFF23 models with the experimentally measured values and found that they have a relative error as low as 5% with the MACE-OFF23(L) model as shown in the supporting Table IX.

D. Water structure and dynamics

A key requirement for bio-organic force fields is an accurate description of water. Several empirical water models have been developed for this purpose, the most common for all-atom biomolecular simulations being TIP3P. Figure 7 shows that MACE-OFF23(M) correctly predicts the radial distribution function (RDF) of water, performing comparably with both TIP3P and the highly accurate MB-pol water model, whose RDF is indistinguishable from experiment [80]. MACE-OFF23(S) gives a qualitatively similar RDF, with one

noticeable shift in the position of the second peak in the $g_{OO}(r)$ peak from 4.5 \AA to 4 \AA . This performance is consistent with the results discussed in more detail in section III F. These interactions are modelled in a purely local way by MACE, having been trained on small water clusters containing up to 50 water molecules. This result further emphasizes the ability of the model to generalize to bulk simulations, even though the training data only contained non-periodic clusters. In contrast, ANI-2X shows a significant over-structuring of the RDF, likely due to the lack of dispersion correction in the underlying quantum mechanical method used to label the training set.

We further calculated the temperature dependence of the density using NPT molecular dynamics simulations, as shown in Figure 9. This is a highly sensitive test for the accuracy of intermolecular interactions [65]. Both the small and medium models over-predict the density to a small extent, which likely originates from the underlying DFT functional or the lack of periodic training data.

Next, we characterize the dynamical properties of water by computing the vibrational density of states, including the IR and Raman spectra selection rules, using MACE models of dipoles and polarizabilities [73]. Given the significant impact of quantum nuclear motion on the dynamics of water [71], we incorporate quantum nuclear effects using the PIGS approach [71] (discussed in Section III C 1), which has a classical cost and has recently been shown to describe quantum nuclear effects in water accurately [81]. As shown in Figure 7, after incorporating quantum nuclear effects, the MACE-OFF23(S) predictions agree with the experiments across the entire frequency range. We note the presence of an overall 2–3 % blue shift with respect to the experiments, consistent with the spectra for paracetamol form II (see Section III C 1). MACE-OFF23(S) even qualitatively captures subtle features of the spectra, including the $0 - 1000\text{ cm}^{-1}$ hydrogen bonding fingerprints in the anisotropic Raman spectrum, and the bimodal nature of the isotropic Raman stretching band arising from the presence of hydrogen-bonded defects in room temperature water.

E. Condensed phase properties of molecular liquids

Small molecule empirical force fields are fitted to reproduce experimental condensed phase properties including densities and heats of vaporization. For machine learning force fields, this task represents a greater challenge, since the potential is typically trained only using QM reference data for isolated molecules and molecular dimers. From these ab initio data, the models learn the long-range interactions necessary to reproduce bulk properties without ever fitting to them.

To investigate the performance of the MACE-OFF23 models in the condensed phase, we selected a bench-

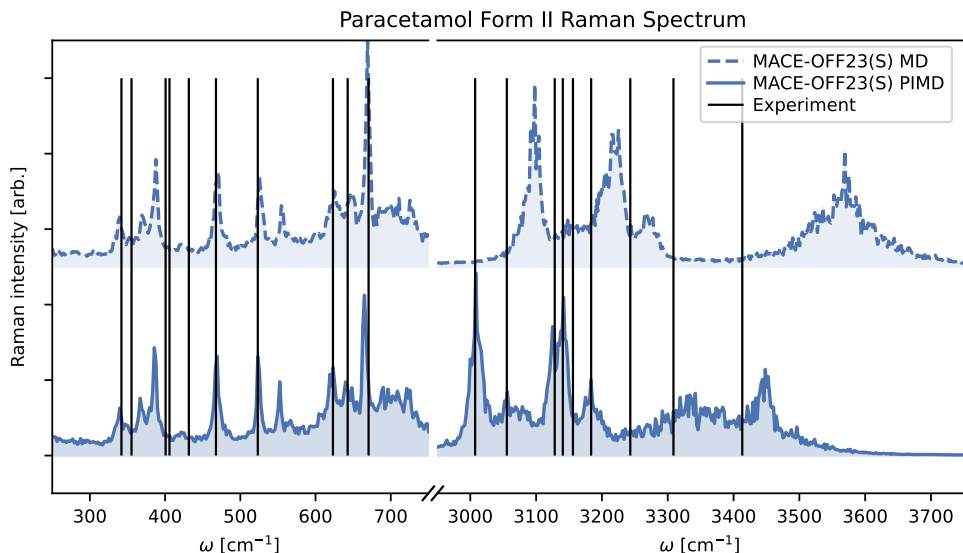


Figure 5. **Powder Raman spectrum of paracetamol form II** [77]. Spectrum computed at ambient conditions using the MACE-OFF23(S) model for the potential energy surface, a MACE model of the polarizability, and a MACE model that incorporates quantum nuclear effects on the potential energy surface using the PIGS approach [71]. The black lines represent experimentally determined band positions [76], scaled by 3% to aid visual comparison with the predicted spectra.

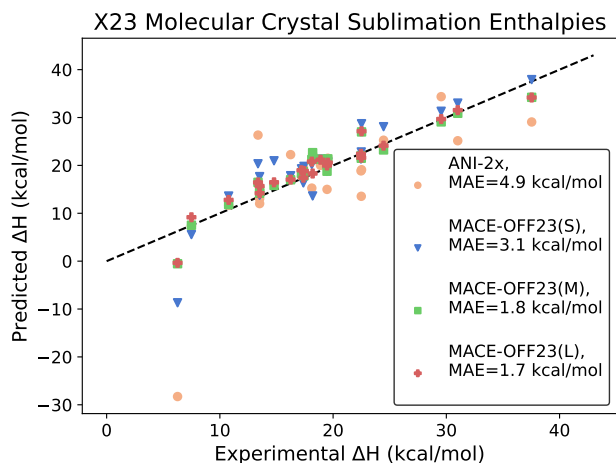


Figure 6. **Sublimation enthalpies of molecular crystals.** Comparison between predicted sublimation enthalpies of the MACE and ANI models and experiment.

mark set of 109 molecules from Ref. [83], containing a representative set of functional groups relevant to medicinal chemistry and biology. MACE-OFF23(M) has a larger receptive field and is therefore better suited for reproducing experimental observables most affected by intermolecular interactions. In general, we found that the small model gave a reasonable description in the NVT ensemble, while the medium model is also able to accurately model liquids in NPT simulations, as detailed below. For the liquid boxes containing approximately 600 atoms, MACE-OFF23(S) achieved a throughput of 2.1×10^6 steps/day via OpenMM on a

single 80GB NVIDIA A100 GPU, whilst the medium model achieved a throughput of 1.1×10^6 steps/day. Meanwhile MACE-OFF23(L) achieved a throughput of 2.8×10^5 steps/day on the same system, highlighting the significant overhead compared to the other two models. See section III G for further discussion of the computational performance.

1. Organic liquids

First, we investigate the predictions of molecular liquid densities under ambient conditions using the medium MACE model shown on the top panel of Figure 8. MACE-OFF23(M) achieves a MAE of 0.09 g/cm^3 , indicating that it can generalize from the intermolecular interactions between molecular dimers in the training set to the condensed phase, retaining a good correlation with experiment. In contrast, the ANI-2x potential has significantly higher errors, with MAE and RMSE errors twice as large as MACE-OFF23(M).

The vast majority of the outliers in the density predictions can be assigned as either low boiling-point ether-containing compounds, polychlorinated hydrocarbons or dibromo-containing compounds. In the first case, this may be due to a marginal under-prediction of the boiling point, since these compounds were simulated at 10 K below their tabulated boiling points. In the latter two cases, this functional group dependence suggests these nonbonded interactions are insufficiently represented in the present training set, which contains, for example, only 84 examples of dibromo-containing dimers. This highlights the need for additional coverage of spe-

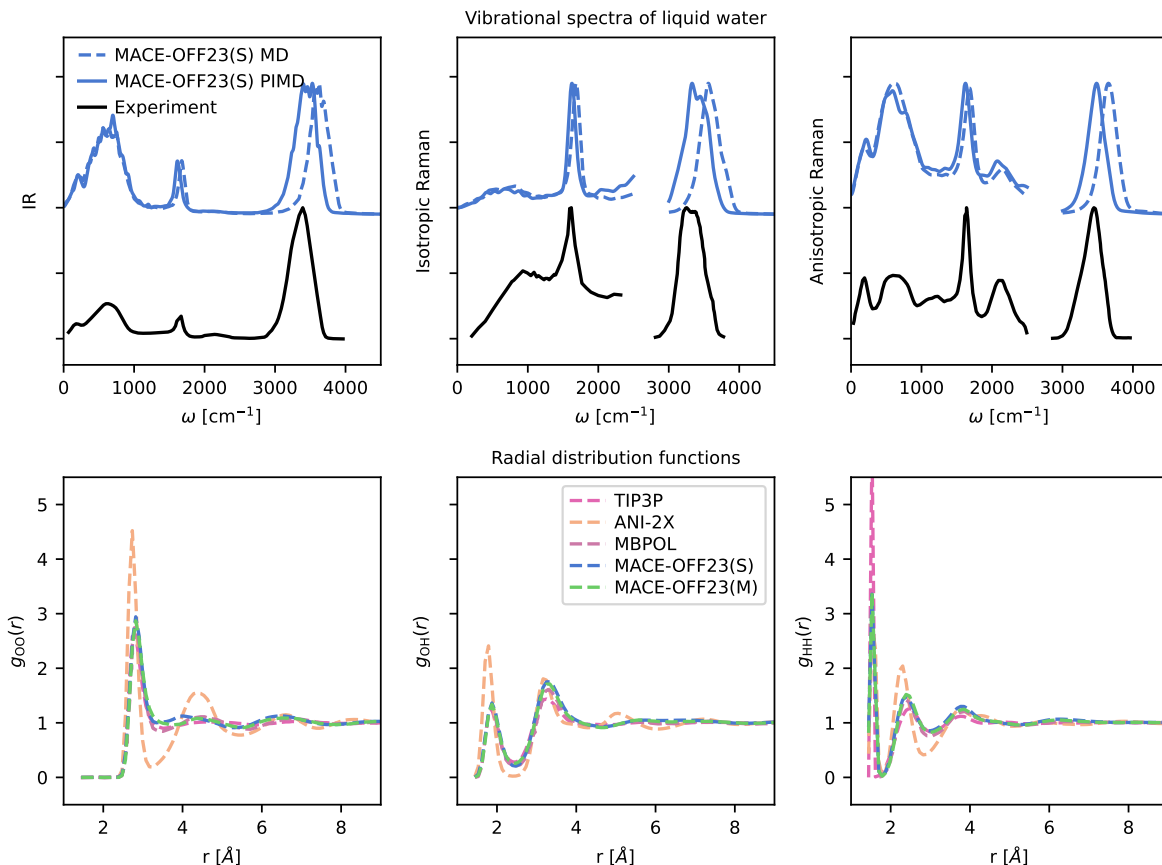


Figure 7. **Water structure and dynamics.** Top: IR, isotropic Raman and anisotropic Raman spectra of water at ambient temperature and density using the MACE-OFF23(S) model for the potential energy surface and a single MACE model of water’s dipole and polarizability [73]. The black curve represents the experiment [82]. The dashed blue curve is obtained from standard (classical) MD, while the solid curve incorporates quantum effects using the PIGS method [71]. Bottom: Radial distribution function of MACE, ANI and TIP3P models. MB-pol traces are reproduced from Ref. [80].

cific functional groups within SPICE (for example, the recent AIMNet2 dataset includes 20 million configurations to cover 14 chemical elements [8]).

Interestingly, we found that MACE-OFF23(S) systematically overpredicts the experimental densities (SI Table VI) with a MAE of 0.23 g/cm^3 . This is likely the result of the slightly higher energy error and the shorter cutoff radius. In particular, the contribution of the intermolecular interactions to the overall energy is much smaller than the intramolecular interactions making the fractional error in them much larger. This is demonstrated in SI Table IV, where the test errors are decomposed into inter- and intramolecular contributions. We find that the medium and large models have significantly lower intermolecular force errors. Whilst we see MACE-OFF23(L) as a replacement for semi-empirical QM due to its relative expense compared to the small and medium models, we nonetheless benchmarked the large model on a small selection of condensed phase systems. We saw comparable performance to the medium model, and in particular observed that compounds that had a high prediction error under the medium model

had a similar error under the large model. This indicates that this error is driven primarily by the dataset rather than by the size of the model, as previously hypothesized.

We further investigate the performance of MACE-OFF23(M) on heats of vaporization. The predictions correlate strongly with the experimental data); however, there is a systematic offset of approximately 2 kcal/mol . We hypothesized that this may result from an underprediction of the total intermolecular interactions originating from two sources: those that appear in molecular dynamics simulations outside the effective cutoff of the MACE model (compare classical simulations, which typically employ long-range corrections to the total energy [84]), and those that the model has not learned from the limited set of intermolecular interactions in the training set.

To investigate this further, we reran the calculations with MACE-OFF24(M) (see SI), which employs an extended cutoff of 6 \AA and has also been trained on additional nonbonded data. We observe a modest decrease in MAE from 2.18 to 1.75 kcal/mol , as well as a small

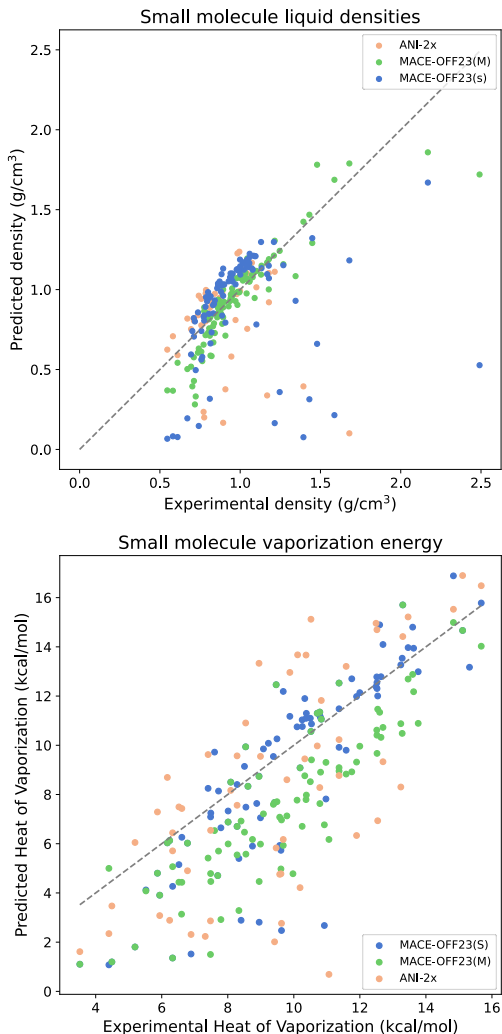


Figure 8. **Molecular liquids.** Comparison between MACE-OFF23(M) and ANI-2x with experiment for densities (top) and heats of vaporization (bottom) of condensed phase organic liquids.

decrease in the accuracy of liquid density predictions. This further reinforces the hypothesis that the poorly predicted densities are a result of under-representation of the functional groups, since the additional training sets do little to increase sampling of these problematic functional groups.

Interestingly, for MACE-OFF23(S), this offset disappears (see SI Table VII), however this is likely due to the overpredicted densities, resulting in a cancellation of errors through overprediction of the magnitude of intermolecular interactions.

Nevertheless, these data indicate that, given a reasonable receptive field and a sufficiently expressive model, it is possible to fit a local force field that captures the interactions required to recover experimental properties.

F. Biomolecular simulations

In the following section, we benchmark the performance of the MACE-OFF models on several well-studied large-scale biomolecular systems. This particular application area is of key interest, and state-of-the-art classical protein force fields have been carefully parameterized over many decades to reproduce key quantum mechanical and thermodynamic properties. However, this extensive parameterization process makes it difficult to extend classical force fields, and overall accuracy and transferability remain fundamentally limited by their functional form. This typically becomes apparent only when each generation of advancing hardware enables sufficiently long simulations to identify issues.

1. Extended cutoff MACE-OFF models

One key observation that emerged from validation of the MACE-OFF23(S) and MACE-OFF23(M) models was an overestimation of the density of liquid water by approximately 20% (Figure 9). Since there is extensive coverage of water clusters in the training set, we hypothesized that this resulted from a missing long-range contribution beyond the receptive field. To investigate this hypothesis, we fitted an additional model, MACE-OFF23(M)b, which has an increased 6 Å layerwise cutoff compared to 5 Å. The larger receptive field leads to a predicted water density within 2% of the experimental value at room temperature.

We also investigated the effect of including additional training data, made up of the Solvated Pubchem and Amino Acid Ligand Pairs datasets from SPICE v2 [63]. Given the direct applicability of these training data to biomolecular simulations, in the following section we test an additional model, MACE-OFF24(M), which includes the additional training data. Given the encouraging performance of MACE-OFF23(M)b, this model also employs the extended 6 Å cutoff.

2. Ala_3 Free Energy Surface

We first investigated the ability of MACE-OFF24(M) to reproduce the free energy surface of the Ala_3 tripeptide. We observed computational performance of 9.6×10^6 steps/day for the vacuum system, and 2.2×10^6 steps/day for the solvated system on an NVIDIA 80GB A100 GPU via the OpenMM interface. Although this remains significantly more expensive than the MM simulation (around 150×10^6 steps/day), it nevertheless enables sufficient sampling of the free energy surface.

Figure 10 shows the free energy surface of Ala_3 in water, modelled by AMBER14/TIP3P and MACE-OFF24(M), respectively. Well-tempered metadynamics was used to enhance sampling along the central ϕ and ψ backbone angles. The AMBER14 simulation

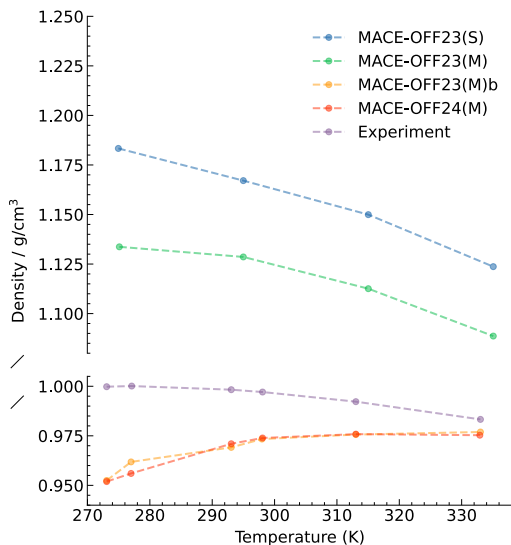


Figure 9. Water density as a function of temperature for the extended cutoff MACE-OFF models

identifies four local minima, corresponding to the anti-parallel β -sheet ($\phi < -120^\circ, \psi > 120^\circ$), a right-handed α -helix ($\phi = -60^\circ, \psi > -60^\circ$), the corresponding left-handed α -helix ($\phi = 60^\circ, \psi > 60^\circ$), and a polyproline II (PPII)-type structure ($\phi = -60^\circ, \psi > 120^\circ$). Comparing the dihedral angle distribution with NMR J-coupling constants, the AMBER14 simulation is generally in good agreement, with a slight overpopulation of both α -helical structures and underpopulation of the PPII mesostate [85]. We therefore use this to enable visual comparison with a well-tuned classical forcefield.

The corresponding MACE simulations show a very similar free energy surface to AMBER14/TIP3P, with the same four local minima identified. Whilst the relative depths of the α -helical conformations are in agreement, AMBER predicts the free energy of the anti-parallel β -sheet to be 1 kcal/mol higher than the PPII minimum, compared to 0.1 kcal/mol for MACE.

We also compare the unbiased conformational ensemble predicted by MACE directly to experiment by calculating 3J coupling constants from the Ramachandran distribution. Computed values are shown in Table III in addition to literature values for AMBER14SB, ANI-2x and experiment [85–87]. MACE-OFF24(M) accurately predicts coupling constants, and is comparable with AMBER14SB. In agreement with our previous findings, both methods significantly outperform ANI-2x, highlighting the difficulties in computing accurate dynamics in the solution phase with MLPs.

3. Folding dynamics of *Ala*₁₅

Having confirmed that MACE-OFF24(M) is capable of recovering the free energy surface of a small peptide, we next investigated the folding of the longer helical

	$^3J(\text{H}_\text{N}, \text{H}_\alpha)$	$^3J(\text{H}_\text{N}, \text{C}_\beta)$	$^3J(\text{H}_\text{N}, \text{C}')_i$
MACE-OFF24(M)	5.70	1.64	1.37
ANI-2x	4.5	1.2	1.4
AMBER14SB	6.07	1.87	1.14
EXP	5.68	2.39	1.29

Table III. **Summary of 3J couplings computed from dihedral distributions.** AMBER14SB and Experimental values taken from Ref. [85]. ANI-2x data taken from Ref. [86].

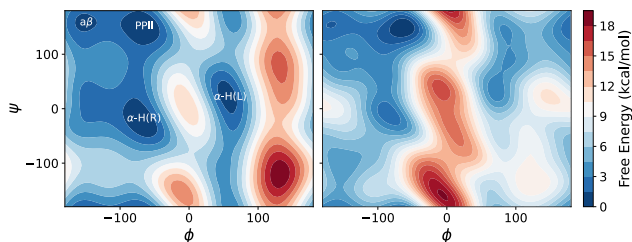


Figure 10. **Free energy surfaces of *Ala*₃ in explicit solvent.** (left) Amber14SB/TIP3P and (right) MACE-OFF24(M).

peptide *Ala*₁₅. Because this is a significantly larger system size than the dipeptide configurations on which the model was trained, this represents a nontrivial test of the extrapolation capability of the potential, including its ability to capture complex hydrogen bonding interactions required to stabilize the secondary structure. Such simulations are believed to be particularly difficult with purely local models such as those in the MACE-OFF family.

As an initial test, the fully extended *Ala*₁₅ structure was simulated *in vacuo*. Figure 11 shows the assignment of the secondary structure during the simulation. The peptide folded within 200 ps, adopting initially a “wavy” intermediate structure, before first folding into a 3_{10} helix. The secondary structure oscillates between the α -helix and the 3_{10} helix for the remainder of the simulation, with the α -helix being the predominant motif. These results are in agreement with other works [9, 39], in which polyalanine peptides are observed to fold through a “wavy intermediate” and oscillate between 3_{10} and α -helices. The oscillatory behaviour has also been observed experimentally [88].

To better understand the performance of MACE-OFF24(M), we compared the predictions to those of MACE-OFF23(M) and MACE-OFF23(M)b. Through ablation studies, we found that both the inclusion of additional training configurations and the increased radial cutoff were required to observe the oscillatory behavior, whilst all other models overstabilize the α -helix, and do not predict the 3_{10} structure. We hypothesize that additional sampling of the nonbonded interactions present in the expanded training set, as well as a larger recep-

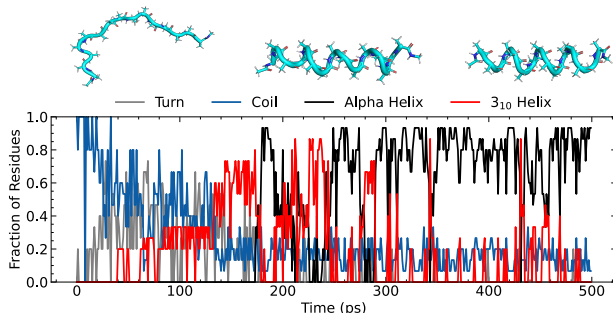


Figure 11. **Ala₁₅ folding dynamics.** Secondary structure assignment during 500 ps trajectory generated with MACE-OFF24(M)FF24M. The structure proceeds via a “wavy” intermediate and oscillates between the α - and 3_{10} helices. Secondary structure assignment was performed with the STRIDE algorithm [90].

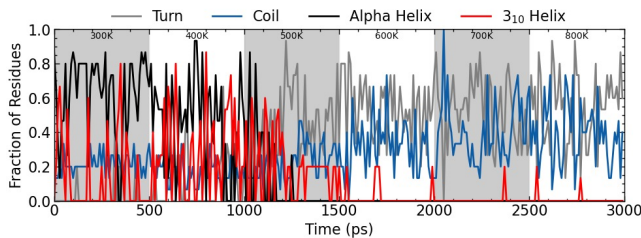


Figure 12. **Ala₁₅ Temperature dependence.** Secondary structure assignment with increasing temperature.

tive field of 12 Å allows the model to learn more subtle hydrogen bonding interactions required to interconvert between the two helical motifs.

We also measured the secondary structure of the peptide as the temperature was increased. Starting from the folded structure at 300K, the temperature was increased in steps from 300K to 900K over the course of 3 ns (Figure 12). The folded structure remains stable up to around 500 K, after which point the helix unfolds and the structure is primarily a random coil. This is an underprediction compared to the experimental unfolding temperature of 725 K, and suggests that there are additional subtle stabilising interactions that are not fully captured by the model [89].

4. Protein simulation in explicit solvent

Finally, we investigated the simulation of a fully solvated protein with MACE-OFF. As a test case, we chose Crambin, a 42 residue threonin storage protein that contains four charged residues. This test goes significantly beyond what can typically be expected from a local force field trained on neutral species only.

Using the MACE-OFF24(M) model, we first confirmed that the force field was indeed capable of simulating a large biomolecular system containing charged

residues. In particular, it has recently been shown that the FENNIX potential fails to simulate a solvated 28 residue peptide due to unphysical proton transfers involving charged residues [37]. We confirmed that the root mean square fluctuations of the protein backbone relative to the minimized structure remained below 1 Å for the duration of a 1 ns simulation, no bond breaking occurred and the secondary structure motifs remained intact (see SI Figure 17).

We then investigated the ability of MACE-OFF24(M) to capture the key vibrational modes of the system. To this end, we prepared a simulation box containing crambin in the high-hydration state, that is, fully solvated in explicit water, for a total system size of approximately 18,000 atoms. The power spectrum was calculated from the final 125 ps of a 1.6 ns simulation recorded at 2 fs resolution, to match the simulation length and sampling frequency employed in Ref [41]. Experimentally, this system has been well studied, and key THz region vibrational modes have been assigned [91]. This system has also been investigated with the AMBER classical force field and several machine learned potentials, including GEMS and, more recently, SO3LR [9, 39, 40]. All three MLPs produce spectra in qualitative agreement with each other. The water peaks at 1640 cm^{-1} and 3200-3600 cm^{-1} are reproduced reasonably accurately, especially considering that no nuclear quantum effects are taken into account (Figure 13). Furthermore, in the terahertz region, two peaks are identified by both GEMS, SO3LR and MACE-OFF24(M). The most obvious of these occurs at 60 cm^{-1} and corresponds to localised internal side chain fluctuations, while a peak at 220 cm^{-1} is due to specific configurations of water at the protein surface.

We note that, whilst a 125 ps trajectory is sufficient to qualitatively identify the spectral features, a much longer simulation of at least several nanoseconds would be required to fully converge the higher frequency THz region of the spectrum and enable full quantitative comparison with experiment, as demonstrated for the GEMS model in Ref. [39]. We note that the power spectrum computed on the final 1.3 ns simulation (discarding the initial 300 ps to equilibration) does not yield a significantly different spectrum to that of the 125 ps simulation used in Figure 13, indicating that significantly more sampling would be required to resolve the THz lineshapes sufficiently to enable experimental comparison.

It is also noteworthy that whilst the three MLPs compared in this section give a qualitatively similar result, their modelling choices are significantly different. Most notably, GEMS and SO3LR explicitly include long-range interactions, whilst MACE is local. Additionally, of these models, both MACE and SO3LR are universal potentials, whilst GEMS is fitted in a system-specific fashion. We mention that, in addition to the GEMS model, the authors benchmarked a variant which was trained only on small fragments, denoted GEMS*, instead of the large system-specific configurations used to

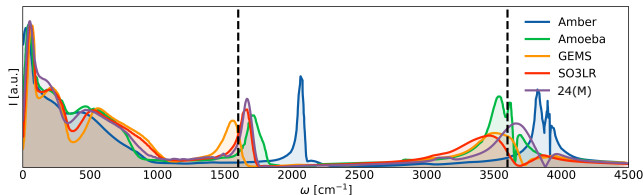


Figure 13. **Protein in explicit solvent.** Power spectrum of the high hydration state of crambin computed from the final 125 ps of a 1.6 ns simulation with MACE-OFF24(M). GEMS, AMBER and SO3LR spectra are reproduced from Ref. [41].

fit GEMS [39]. The power spectrum produced by this model is also in qualitative agreement with the other ML potentials, however, the RMSD is reduced, indicating the protein structure is confined to small fluctuations around local minima. This model also fails to reproduce experimental observables of other biomolecular systems, for example Ala₁₅ is not predicted to fold under the GEMS* potential, suggesting the top-down fragments are required to accurately reproduce nonbonded interactions within the GEMS family of models.

The results of sections III E and III F highlight the most significant differences between previous transferable organic ML potentials and the MACE-OFF models. These are, to our knowledge, the first local ML potentials capable of reproducing experimental properties of condensed phase molecular systems, as well as large-scale, all-atom, explicit solvent biomolecular simulations without relying on augmented, system-specific training data.

G. Computational performance

To evaluate the computational performance of the MACE-OFF models, we performed NVT molecular dynamics for water using both OpenMM and LAMMPS, with simulation boxes ranging from 10^2 to 10^5 atoms. The OpenMM results shown in Figure 14 were collected with a single NVIDIA A100 80GB GPU. The LAMMPS results shown in Figures 15-16 highlight both CPU and GPU evaluation.

In addition to the native PyTorch implementations of the MACE-OFF23 models, we also report results for optimized implementations leveraging custom C++, CUDA, and/or Kokkos code. One optimized variant, MACE-OFF23(S)-OPT, incorporates custom CUDA kernels which are packaged as a standalone, inference-only library, `cuda_mace` [92]. Another pure-C++ implementation, as well as a Kokkos implementation, will be made available as part of the `symmetrix` library [93].

In these optimized variants, the learnable radial function $R_{k\eta_1 l_1 l_2 l_3}^{(t)}(r_{ij})$ is evaluated with cubic splines, which efficiently map r_{ij} to each of the outputs of the radial MLP. Furthermore, Eqs. 2 and 3 are implemented in unified kernels that simultaneously compute the one-

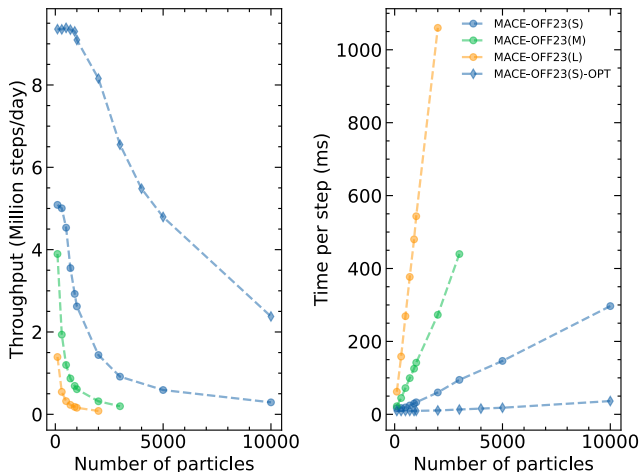


Figure 14. **Performance in OpenMM.** Performance of MACE-OFF23 in OpenMM for liquid water in the NVT ensemble at 1 g/cm^3 at 300K with a 1 fs timestep on a single NVIDIA 80GB A100 GPU.

particle basis and perform the summation over neighbors to generate the invariant atomic basis A_i . The computation of spherical harmonics, as detailed in equation 2 is accelerated using the `sphericart` [94] library, which offers a highly optimized implementation for real spherical harmonics. All linear and equivariant linear operations have been substituted with custom kernels, and the `cuda_mace` implementation further leverages tensor core acceleration while incorporating error-correction techniques to ensure numerical accuracy. Additionally, the computation of the product basis \mathbf{B}_i in equation 4 is optimized using the sparsity of the generalized Clebsch-Gordon coefficients $C_{\eta,lm}^{LM}$, significantly accelerating the product calculations over both the body order v and the coupling terms.

IV. Outlook

In this paper, we presented the series of MACE-OFF force field and dipole models, demonstrating the broad applicability, transferability and capability of purely short-range machine learning potentials for organic (bio)molecular simulations. We have shown that the models, based on the MACE higher order equivariant message passing architecture, can improve on the pioneering ANI models [27] that served as the only widely applicable machine learning force fields for molecules for a number of years. While a full ablation study between different ML models is not possible due to a wide range of design choices made in their construction, the MACE-OFF model architecture, training data and loss function all contribute to significant improvements in both accuracy and extrapolation, combined with high computational speed.

The lack of explicit long-range interactions limits the domain of applicability of the present model to neutral,

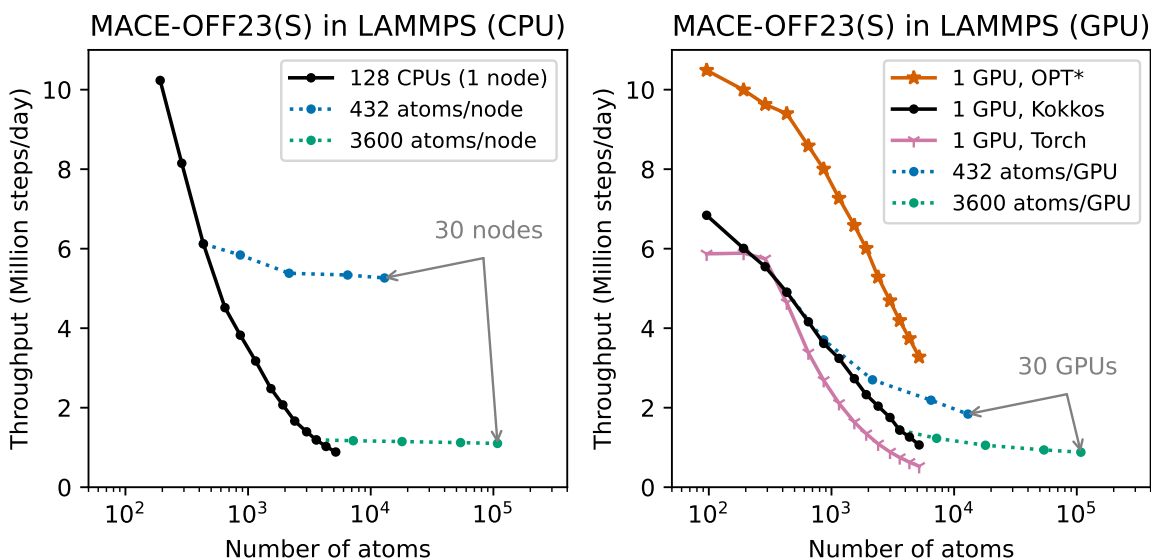


Figure 15. **Throughput in LAMMPS.** Performance of molecular dynamics in LAMMPS for water in the NVT ensemble at 1 g/cm³ and 300 K with a 1 fs timestep. All simulations used variants of the MACE-OFF23(S) model.

The left panel highlights CPU performance achievable on the UK-based Archer2 CPU supercomputer, using the new pure-C++ MACE implementation. The solid black curve demonstrates the throughput of a single 128-core node as a function of the number of atoms. The two dotted curves demonstrate weak scaling with 432 atoms/node or 3600 atoms/node. All calculations used double precision floating point numbers.

The right panel demonstrates the performance of the GPU evaluators. The three solid curves provide single-GPU results (determined with NVIDIA A100 80GB GPUs) for the native Torch-based MACE-OFF23(S), a custom Kokkos-based MACE implementation, and the `cuda_mace` implementation marked as OPT*. The asterisk indicates that these latter simulations used single precision floating point numbers, with error correction for the most numerically sensitive terms, in contrast to the remaining calculations which were performed with double precision. Finally, the two dashed curves demonstrate the performance when multiple GPUs are employed, using the pure-Kokkos implementation, to access larger systems with domain decomposition. More work is needed to improve this weak scaling.

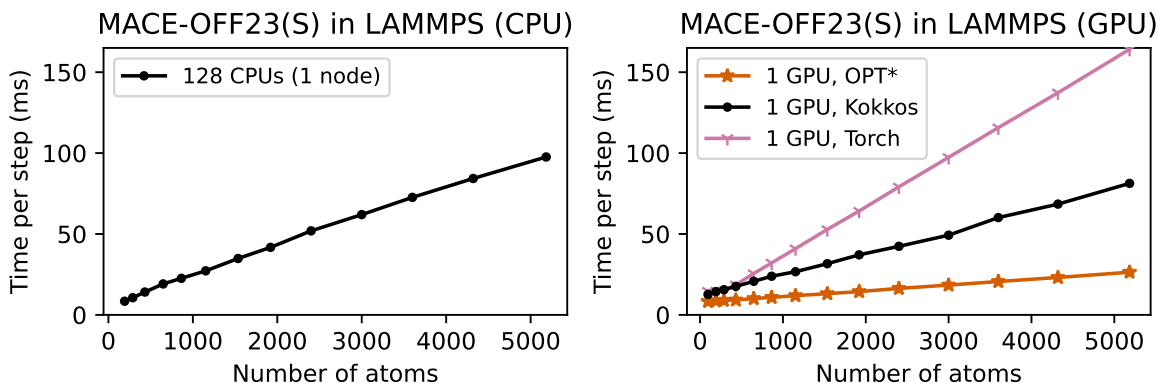


Figure 16. **Evaluation speed in LAMMPS.** Data from Figure 15, replotted to show the average duration of each timestep.

non-radical and non-reactive systems. This is something that the recently published AIMNet2 model aims to address by extending the ANI models to include charged species and long-range interactions [8]. We are currently working on a next-generation MACE-OFF

model that will similarly include an explicit description of charges, enabling the description of amino acids with different protonation states, charged nucleic acids, and counter-ions. This will pave the way towards obtaining an accurate quantum mechanical transferable machine

learning force field for simulating the full range of biologically relevant systems.

Acknowledgements

DPK acknowledges support from AstraZeneca and the EPSRC. DJC and JH acknowledge support from a UKRI Future Leaders Fellowship (grant MR/T019654/1). V.K. acknowledges support from the Ernest Oppenheimer Early Career Fellowship, the Sydney Harvey Junior Research Fellowship, Churchill College, University of Cambridge, and UCL’s startup funds. W.C.W. acknowledges support from the EPSRC (Grant EP/V062654/1), as well as an engagement from the Virtual Institute for Scientific Software at Georgia Tech, funded by Schmidt Sciences. In particular, Ketan Bhardwaj and Dave Brownwell of the Georgia Tech Scientific Software Engineering Center contributed to the Kokkos-based MACE evaluator. JHM acknowledges support from an AstraZeneca Non-Clinical PhD studentship, and thanks Prof. Ola Engkvist, Dr Marco Klähn and Dr Graeme Robb from AstraZeneca for their helpful discussions and supervision. The authors also thank Christoph Schran for providing the carved water cluster geometries. We also thank Dr Peter Eastman and Dr Stephen Farr for their help implementing the MACE-OpenMM interface.

We are grateful for computational support from the Swiss National Supercomputing Centre under project s1209, UCL Myriad High Performance Computing Facility, the Rocket High Performance Computing service at Newcastle University, the UK national high-performance computing service, ARCHER2, for which access was obtained via the UKCP consortium and EPSRC grant EP/P022561/1, the Cambridge Service for Data Driven Discovery (CSD3), obtained through a University of Cambridge EPSRC Core Equipment Award (EP/X034712/1), and Ångström AI.

Contributions

DPK conceived the project, curated the training data, trained and evaluated the models, ran parts of the torsion drive tests, the molecular crystal tests, fitted the dipole and polarisability models for water and paracetamol bulk systems, and wrote the initial draft. JHM and DPK implemented the OpenMM interface. JHM trained and evaluated the models, curated the datasets, performed experiments on molecular liquids, peptides and proteins, benchmarked the model performance in OpenMM and wrote the initial draft. JTH implemented the MACE-torsion drive interfaces, and ran the DFT and force field torsion drives. VK fitted the MACE-OFF23- μ , performed the MD and PIMD simulations of water and molecular crystals and produced their IR and Raman spectra. YP performed the error analysis for the MACE-OFF23- μ model and performed MD and PIMD simulations and calculated the IR spectrum of paracetamol molecule. IB and NJB implemented the accelerated custom kernels, and the `cuda_mace` library is maintained by NJB. WCW implemented the MACE-LAMMPS interface, wrote the pure C++ and Kokkos implementations, and benchmarked the model performance in LAMMPS. IBM developed the intermolecular error analysis and evaluated the models. DJC and GC supervised the project. All authors discussed the results and edited the final manuscript.

Data Availability

The data used to train the models are publicly available at: <https://doi.org/10.17863/CAM.107498>. The torsion drive dataset is also available at: <https://zenodo.org/records/11385284>. The MACE-OFF series of models are available at: <https://github.com/ACEsuit/mace-off/tree/main> and the MACE-OFF23- μ model is available at: <https://github.com/venkatkapil24/MACE-OFF-mu-models>

-
- [1] Y. Lysogorskiy, C. v. d. Oord, A. Bochkarev, S. Menon, M. Rinaldi, T. Hammerschmidt, M. Mrovec, A. Thompson, G. Csányi, C. Ortner, *et al.*, Performant implementation of the atomic cluster expansion (pace) and application to copper and silicon, *npj computational materials* **7**, 97 (2021).
- [2] I. Batatia, D. P. Kovacs, G. Simm, C. Ortner, and G. Csányi, Mace: Higher order equivariant message passing neural networks for fast and accurate force fields, *Advances in Neural Information Processing Systems* **35**, 11423 (2022).
- [3] D. P. Kovács, I. Batatia, E. S. Arany, and G. Csányi, Evaluation of the MACE force field architecture: From medicinal chemistry to materials science, *The Journal of Chemical Physics* **159**, 044118 (2023).
- [4] S. Batzner, A. Musaelian, L. Sun, M. Geiger, J. P. Mailoa, M. Kornbluth, N. Molinari, T. E. Smidt, and B. Kozinsky, E (3)-equivariant graph neural networks for data-efficient and accurate interatomic potentials, *Nature communications* **13**, 2453 (2022).
- [5] V. Zaverkin, D. Holzmüller, L. Bonferraro, and J. Kästner, Transfer learning for chemically accurate interatomic neural network potentials, *Physical Chemistry Chemical Physics* **25**, 5383 (2023).
- [6] M. Haghightlari, J. Li, X. Guan, O. Zhang, A. Das, C. J. Stein, F. Heidar-Zadeh, M. Liu, M. Head-Gordon, L. Bertels, *et al.*, Newtonnet: A newtonian message passing network for deep learning of interatomic potentials and forces, *Digital Discovery* **1**, 333 (2022).

- [7] A. V. Shapeev, Moment tensor potentials: A class of systematically improvable interatomic potentials, *Multiscale Modeling & Simulation* **14**, 1153 (2016).
- [8] D. Anstine, R. Zubatyuk, and O. Isayev, Aimnet2: A neural network potential to meet your neutral, charged, organic, and elemental-organic needs, *ChemRxiv 10.26434/chemrxiv-2023-296ch* (2023).
- [9] A. Kabylda, V. Vassilev-Galindo, S. Chmiela, I. Poltavsky, and A. Tkatchenko, Efficient interatomic descriptors for accurate machine learning force fields of extended molecules, *Nature Communications* **14**, 3562 (2023).
- [10] J. Behler, Four generations of high-dimensional neural network potentials, *Chemical Reviews* **121**, 10037 (2021).
- [11] F. Musil, A. Grisafi, A. P. Bartók, C. Ortner, G. Csányi, and M. Ceriotti, Physics-inspired structural representations for molecules and materials, *Chemical Reviews* **121**, 9759 (2021).
- [12] V. L. Deringer, A. P. Bartók, N. Bernstein, D. M. Wilkins, M. Ceriotti, and G. Csányi, Gaussian process regression for materials and molecules, *Chemical Reviews* **121**, 10073 (2021).
- [13] B. Huang and O. A. Von Lilienfeld, Ab initio machine learning in chemical compound space, *Chemical reviews* **121**, 10001 (2021).
- [14] M. S. Daw and M. I. Baskes, Embedded-atom method: Derivation and application to impurities, surfaces, and other defects in metals, *Physical Review B* **29**, 6443 (1984).
- [15] V. L. Deringer, N. Bernstein, G. Csányi, C. Ben Mahmoud, M. Ceriotti, M. Wilson, D. A. Drabold, and S. R. Elliott, Origins of structural and electronic transitions in disordered silicon, *Nature* **589**, 59 (2021).
- [16] W. J. Baldwin, X. Liang, J. Klarbring, M. Dubajic, D. Dell’Angelo, C. Sutton, C. Caddeo, S. D. Stranks, A. Mattoni, A. Walsh, *et al.*, Dynamic local structure in caesium lead iodide: Spatial correlation and transient domains, *Small*, 2303565 (2023).
- [17] C. W. Rosenbrock, K. Gubaev, A. V. Shapeev, L. B. Pártay, N. Bernstein, G. Csányi, and G. L. Hart, Machine-learned interatomic potentials for alloys and alloy phase diagrams, *npj Computational Materials* **7**, 24 (2021).
- [18] Y. Zhou, W. Zhang, E. Ma, and V. L. Deringer, Device-scale atomistic modelling of phase-change memory materials, *Nature Electronics*, 1 (2023).
- [19] P. Dauber-Osguthorpe and A. T. Hagler, Biomolecular force fields: where have we been, where are we now, where do we need to go and how do we get there?, *J Comput Aided Mol Des* **33**, 133–203 (2019).
- [20] A. T. Hagler, Force field development phase ii: Relaxation of physics-based criteria... or inclusion of more rigorous physics into the representation of molecular energetics, *J Comput Aided Mol Des* **33**, 205–264 (2019).
- [21] S. Boothroyd, P. K. Behara, O. C. Madin, D. F. Hahn, H. Jang, V. Gapsys, J. R. Wagner, J. T. Horton, D. L. Dotson, M. W. Thompson, J. Maat, T. Gokey, L.-P. Wang, D. J. Cole, M. K. Gilson, J. D. Chodera, C. I. Bayly, M. R. Shirts, and D. L. Mobley, Development and benchmarking of open force field 2.0.0: The sage small molecule force field, *J. Chem. Theory Comput.* **0**, null (2023), pMID: 37167319.
- [22] V. Gapsys, L. Pérez-Benito, M. Aldeghi, D. Seeliger, H. Van Vlijmen, G. Tresadern, and B. L. De Groot, Large scale relative protein ligand binding affinities using non-equilibrium alchemy, *Chem. Sci.* **11**, 1140 (2020).
- [23] C. Bannwarth, S. Ehlert, and S. Grimme, Gfn2-xtb—an accurate and broadly parametrized self-consistent tight-binding quantum chemical method with multipole electrostatics and density-dependent dispersion contributions, *Journal of chemical theory and computation* **15**, 1652 (2019).
- [24] J. S. Smith, O. Isayev, and A. E. Roitberg, Ani-1: an extensible neural network potential with dft accuracy at force field computational cost, *Chemical science* **8**, 3192 (2017).
- [25] J. S. Smith, B. Nebgen, N. Lubbers, O. Isayev, and A. E. Roitberg, Less is more: Sampling chemical space with active learning, *The Journal of chemical physics* **148**, 241733 (2018).
- [26] J. S. Smith, B. T. Nebgen, R. Zubatyuk, N. Lubbers, C. Devereux, K. Barros, S. Tretiak, O. Isayev, and A. E. Roitberg, Approaching coupled cluster accuracy with a general-purpose neural network potential through transfer learning, *Nature communications* **10**, 1 (2019).
- [27] C. Devereux, J. S. Smith, K. K. Huddleston, K. Barros, R. Zubatyuk, O. Isayev, and A. E. Roitberg, Extending the applicability of the ani deep learning molecular potential to sulfur and halogens, *Journal of Chemical Theory and Computation* **16**, 4192 (2020).
- [28] R. Zubatyuk, J. S. Smith, J. Leszczynski, and O. Isayev, Accurate and transferable multitask prediction of chemical properties with an atoms-in-molecules neural network, *Science advances* **5**, eaav6490 (2019).
- [29] R. Zubatyuk, J. S. Smith, B. T. Nebgen, S. Tretiak, and O. Isayev, Teaching a neural network to attach and detach electrons from molecules, *Nature Communications* **12**, 4870 (2021).
- [30] J. Behler and M. Parrinello, Generalized neural-network representation of high-dimensional potential-energy surfaces, *Physical review letters* **98**, 146401 (2007).
- [31] J. S. Smith, O. Isayev, and A. E. Roitberg, Ani-1, a data set of 20 million calculated off-equilibrium conformations for organic molecules, *Scientific data* **4**, 1 (2017).
- [32] J. S. Smith, R. Zubatyuk, B. Nebgen, N. Lubbers, K. Barros, A. E. Roitberg, O. Isayev, and S. Tretiak, The ani-1ccx and ani-1x data sets, coupled-cluster and density functional theory properties for molecules, *Scientific data* **7**, 134 (2020).
- [33] T. J. Inizan, T. Plé, O. Adjoua, P. Ren, H. Gökcan, O. Isayev, L. Lagardère, and J.-P. Piquemal, Scalable hybrid deep neural networks/polarizable potentials biomolecular simulations including long-range effects, *Chemical Science* **14**, 5438 (2023).
- [34] N. T. P. Tu, N. Rezaiooei, E. R. Johnson, and C. Rowley, A neural network potential with rigorous treatment of long-range dispersion, *Digital Discovery* (2023).
- [35] J. Gilmer, S. S. Schoenholz, P. F. Riley, O. Vinyals, and G. E. Dahl, Neural message passing for quantum chemistry, in *International conference on machine learning* (PMLR, 2017) pp. 1263–1272.

- [36] O. T. Unke and M. Meuwly, Physnet: A neural network for predicting energies, forces, dipole moments, and partial charges, *Journal of chemical theory and computation* **15**, 3678 (2019).
- [37] T. Plé, L. Lagardère, and J.-P. Piquemal, Force-field-enhanced neural network interactions: from local equivariant embedding to atom-in-molecule properties and long-range effects, *Chemical Science* 10.1039/d3sc02581k (2023).
- [38] M. Thürlmann and S. Riniker, Hybrid classical/machine-learning force fields for the accurate description of molecular condensed-phase systems, *Chemical Science* **14**, 12661 (2023).
- [39] O. T. Unke, M. Stöhr, S. Ganscha, T. Unterthiner, H. Maennel, S. Kashubin, D. Ahlin, M. Gastegger, L. M. Sandonas, J. T. Berryman, A. Tkatchenko, and K.-R. Müller, Biomolecular dynamics with machine-learned quantum-mechanical force fields trained on diverse chemical fragments, *Science Advances* **10**, eadn4397 (2024), <https://www.science.org/doi/pdf/10.1126/sciadv.adn4397>.
- [40] O. T. Unke, S. Chmiela, M. Gastegger, K. T. Schütt, H. E. Sauceda, and K.-R. Müller, Spookynet: Learning force fields with electronic degrees of freedom and non-local effects, *Nature communications* **12**, 7273 (2021).
- [41] A. Kabylda, J. T. Frank, S. S. Dou, A. Khabibrakhmanov, L. M. Sandonas, O. T. Unke, S. Chmiela, K.-R. Müller, and A. Tkatchenko, Molecular Simulations with a Pretrained Neural Network and Universal Pairwise Force Fields (2024).
- [42] K. Schütt, P.-J. Kindermans, H. E. Sauceda Felix, S. Chmiela, A. Tkatchenko, and K.-R. Müller, Schnet: A continuous-filter convolutional neural network for modeling quantum interactions, *Advances in neural information processing systems* **30** (2017).
- [43] K. Schütt, O. Unke, and M. Gastegger, Equivariant message passing for the prediction of tensorial properties and molecular spectra, in *International Conference on Machine Learning* (PMLR, 2021) pp. 9377–9388.
- [44] J. Gastegger, F. Becker, and S. Günnemann, Gemnet: Universal directional graph neural networks for molecules, *Advances in Neural Information Processing Systems* **34**, 6790 (2021).
- [45] M. J. Willatt, F. Musil, and M. Ceriotti, Feature optimization for atomistic machine learning yields a data-driven construction of the periodic table of the elements, *Physical Chemistry Chemical Physics* **20**, 29661 (2018).
- [46] J. P. Darby, D. P. Kovács, I. Batatia, M. A. Caro, G. L. Hart, C. Ortner, and G. Csányi, Tensor-reduced atomic density representations, *Physical Review Letters* **131**, 028001 (2023).
- [47] E. Wigner, *Group theory: and its application to the quantum mechanics of atomic spectra*, Vol. 5 (Elsevier, 2012).
- [48] G. Dussan, M. Bachmayr, G. Csányi, R. Drautz, S. Etter, C. van der Oord, and C. Ortner, Atomic cluster expansion: Completeness, efficiency and stability, *Journal of Computational Physics* **454**, 110946 (2022).
- [49] I. Batatia, S. Batzner, D. P. Kovács, A. Musaelian, G. N. Simm, R. Drautz, C. Ortner, B. Kozinsky, and G. Csányi, The design space of e (3)-equivariant atom-centered interatomic potentials, arXiv preprint arXiv:2205.06643 (2022).
- [50] D. P. Kovács, C. v. d. Oord, J. Kucera, A. E. Allen, D. J. Cole, C. Ortner, and G. Csányi, Linear atomic cluster expansion force fields for organic molecules: beyond rmse, *Journal of chemical theory and computation* **17**, 7696 (2021).
- [51] P. Eastman, P. K. Behara, D. L. Dotson, R. Galvelis, J. E. Herr, J. T. Horton, Y. Mao, J. D. Chodera, B. P. Pritchard, Y. Wang, *et al.*, Spice, a dataset of drug-like molecules and peptides for training machine learning potentials, *Scientific Data* **10**, 11 (2023).
- [52] A. Najibi and L. Goerigk, The nonlocal kernel in van der waals density functionals as an additive correction: An extensive analysis with special emphasis on the b97m-v and ω b97m-v approaches, *Journal of Chemical Theory and Computation* **14**, 5725 (2018).
- [53] F. Weigend and R. Ahlrichs, Balanced basis sets of split valence, triple zeta valence and quadruple zeta valence quality for h to rn: Design and assessment of accuracy, *Physical Chemistry Chemical Physics* **7**, 3297 (2005).
- [54] D. Rappoport and F. Furche, Property-optimized gaussian basis sets for molecular response calculations, *The Journal of chemical physics* **133** (2010).
- [55] S. Grimme, S. Ehrlich, and L. Goerigk, Effect of the damping function in dispersion corrected density functional theory, *Journal of computational chemistry* **32**, 1456 (2011).
- [56] S. Grimme, J. Antony, S. Ehrlich, and H. Krieg, A consistent and accurate ab initio parametrization of density functional dispersion correction (dft-d) for the 94 elements h-pu, *The Journal of chemical physics* **132** (2010).
- [57] D. G. Smith, L. A. Burns, A. C. Simmonett, R. M. Parrish, M. C. Schieber, R. Galvelis, P. Kraus, H. Kruse, R. Di Remigio, A. Alenaizan, *et al.*, Psi4 1.4: Open-source software for high-throughput quantum chemistry, *The Journal of chemical physics* **152** (2020).
- [58] J. A. Maier, C. Martinez, K. Kasavajhala, L. Wickstrom, K. E. Hauser, and C. Simmerling, ff14sb: improving the accuracy of protein side chain and backbone parameters from ff99sb, *Journal of chemical theory and computation* **11**, 3696 (2015).
- [59] A. G. Donchev, A. G. Taube, E. Decolvenaere, C. Hargus, R. T. McGibbon, K.-H. Law, B. A. Gregersen, J.-L. Li, K. Palmo, K. Siva, *et al.*, Quantum chemical benchmark databases of gold-standard dimer interaction energies, *Scientific data* **8**, 55 (2021).
- [60] C. Isert, K. Atz, J. Jiménez-Luna, and G. Schneider, Qmugs, quantum mechanical properties of drug-like molecules, *Scientific Data* **9**, 273 (2022).
- [61] J. P. Darby, D. P. Kovács, I. Batatia, M. A. Caro, G. L. Hart, C. Ortner, and G. Csányi, Tensor-reduced atomic density representations, *Physical Review Letters* **131**, 028001 (2023).
- [62] C. Schran, F. L. Thiemann, P. Rowe, E. A. Müller, O. Marsalek, and A. Michaelides, Machine learning potentials for complex aqueous systems made simple, *Proceedings of the National Academy of Sciences* **118**, e2110077118 (2021).
- [63] P. Eastman, P. K. Behara, D. Dotson, R. Galvelis, J. Herr, J. Horton, Y. Mao, J. Chodera, B. Pritchard, Y. Wang, G. De Fabritiis, and T. Markland, Spice 2.0.1, 10.5281/zenodo.10975225 (2024).

- [64] A. Paszke, S. Gross, F. Massa, A. Lerer, J. Bradbury, G. Chanan, T. Killeen, Z. Lin, N. Gimeshain, L. Antiga, A. Desmaison, A. Köpf, E. Yang, Z. DeVito, M. Raison, A. Tejani, S. Chilamkurthy, B. Steiner, L. Fang, J. Bai, and S. Chintala, Pytorch: An imperative style, high-performance deep learning library, in *Neural Information Processing Systems* (2019).
- [65] I.-B. Magdău, D. J. Arismendi-Arrieta, H. E. Smith, C. P. Grey, K. Hermansson, and G. Csányi, Machine learning force fields for molecular liquids: Ethylene carbonate/ethyl methyl carbonate binary solvent, *npj Computational Materials* **9**, 146 (2023).
- [66] P. Pracht, Y. Pillai, V. Kapil, G. Csányi, N. Gönheimer, M. Vondrák, J. T. Margraf, and D. J. Wales, Efficient composite infrared spectroscopy: Combining the double-harmonic approximation with machine learning potentials, *Journal of Chemical Theory and Computation* **20**, 10986–11004 (2024).
- [67] J. T. Horton, S. Boothroyd, J. Wagner, J. A. Mitchell, T. Gokey, D. L. Dotson, P. K. Behara, V. K. Ramaswamy, M. Mackey, J. D. Chodera, *et al.*, Open force field bespokefit: Automating bespoke torsion parametrization at scale, *Journal of Chemical Information and Modeling* **62**, 5622 (2022).
- [68] D. Hao, X. He, A. E. Roitberg, S. Zhang, and J. Wang, Development and evaluation of geometry optimization algorithms in conjunction with ani potentials, *Journal of Chemical Theory and Computation* **18**, 978 (2022).
- [69] S.-L. J. Lahey, T. N. Thien Phuc, and C. N. Rowley, Benchmarking force field and the ani neural network potentials for the torsional potential energy surface of biaryl drug fragments, *Journal of Chemical Information and Modeling* **60**, 6258 (2020).
- [70] B. K. Rai, V. Sresht, Q. Yang, R. Unwalla, M. Tu, A. M. Mathiowetz, and G. A. Bakken, Torsionnet: A deep neural network to rapidly predict small-molecule torsional energy profiles with the accuracy of quantum mechanics, *Journal of Chemical Information and Modeling* **62**, 785 (2022).
- [71] F. Musil, I. Zaporozhets, F. Noé, C. Clementi, and V. Kapil, Quantum dynamics using path integral coarse-graining, *The Journal of Chemical Physics* **157**, 10.1063/5.0120386 (2022).
- [72] d. NIST Mass Spectrometry Data Center, William E. Wallace, Infrared spectra (2025), retrieved January 20, 2025.
- [73] V. Kapil, D. P. Kovács, G. Csányi, and A. Michaelides, First-principles spectroscopy of aqueous interfaces using machine-learned electronic and quantum nuclear effects, *Faraday Discussions* 10.1039/d3fd00113j (2023).
- [74] N. Raimbault, A. Grisafi, M. Ceriotti, and M. Rossi, Using gaussian process regression to simulate the vibrational raman spectra of molecular crystals, *New Journal of Physics* **21**, 105001 (2019).
- [75] N. Raimbault, A. Grisafi, M. Ceriotti, and M. Rossi, Using gaussian process regression to simulate the vibrational raman spectra of molecular crystals, *New Journal of Physics* **21**, 105001 (2019).
- [76] B. A. Kolesov, M. A. Mikhailenko, and E. V. Boldyreva, Dynamics of the intermolecular hydrogen bonds in the polymorphs of paracetamol in relation to crystal packing and conformational transitions: a variable-temperature polarized raman spectroscopy study, *Physical Chemistry Chemical Physics* **13**, 14243 (2011).
- [77] N. Raimbault, V. Athavale, and M. Rossi, Anharmonic effects in the low-frequency vibrational modes of aspirin and paracetamol crystals, *Physical Review Materials* **3**, 10.1103/physrevmaterials.3.053605 (2019).
- [78] A. M. Reilly and A. Tkatchenko, Understanding the role of vibrations, exact exchange, and many-body van der waals interactions in the cohesive properties of molecular crystals, *The Journal of chemical physics* **139**, 024705 (2013).
- [79] G. A. Dolgonos, J. Hoja, and A. D. Boese, Revised values for the x23 benchmark set of molecular crystals, *Physical Chemistry Chemical Physics* **21**, 24333 (2019).
- [80] G. R. Medders, V. Babin, and F. Paesani, Development of a “First-Principles” Water Potential with Flexible Monomers. III. Liquid Phase Properties, *Journal of Chemical Theory and Computation* **10**, 2906 (2014).
- [81] M. Ceriotti, W. Fang, P. G. Kusalik, R. H. McKenzie, A. Michaelides, M. A. Morales, and T. E. Markland, Nuclear quantum effects in water and aqueous systems: Experiment, theory, and current challenges, *Chemical Reviews* **116**, 7529–7550 (2016).
- [82] A. K. Soper, The radial distribution functions of water as derived from radiation total scattering experiments: Is there anything we can say for sure?, *ISRN Physical Chemistry* **2013**, 1–67 (2013).
- [83] J. T. Horton, A. E. Allen, L. S. Dodda, and D. J. Cole, Qubekit: Automating the derivation of force field parameters from quantum mechanics, *Journal of chemical information and modeling* **59**, 1366 (2019).
- [84] M. R. Shirts, D. L. Mobley, J. D. Chodera, and V. S. Pande, Accurate and efficient corrections for missing dispersion interactions in molecular simulations, *The Journal of Physical Chemistry B* **111**, 13052 (2007).
- [85] S. Zhang, R. Schweitzer-Stenner, and B. Urbanc, Do Molecular Dynamics Force Fields Capture Conformational Dynamics of Alanine in Water?, *Journal of Chemical Theory and Computation* **16**, 510 (2020).
- [86] D. Rosenberger, J. S. Smith, and A. E. Garcia, Modeling of peptides with classical and novel machine learning force fields: A comparison, *The Journal of Physical Chemistry B* **125**, 3598 (2021).
- [87] J.-S. Hu and A. Bax, Determination of φ and $X1$ Angles in Proteins from ^{13}C - ^{13}C Three-Bond J Couplings Measured by Three-Dimensional Heteronuclear NMR. How Planar Is the Peptide Bond?, *Journal of the American Chemical Society* **119**, 6360 (1997).
- [88] K. A. Bolin and G. L. Millhauser, α and β : The Split Personality of Polypeptide Helices, *Accounts of Chemical Research* **32**, 1027 (1999).
- [89] M. Kohtani, T. C. Jones, J. E. Schneider, and M. F. Jarrold, Extreme Stability of an Unsolvated α -Helix, *Journal of the American Chemical Society* **126**, 7420 (2004).
- [90] M. Heinig and D. Frishman, STRIDE: A web server for secondary structure assignment from known atomic coordinates of proteins, *Nucleic Acids Research* **32**, W500 (2004).
- [91] K. N. Woods, The glassy state of crambin and the THz time scale protein-solvent fluctuations possibly related to protein function, *BMC Biophysics* **7**, 8 (2014).

- [92] N. J. Browning, Cuda mace, https://github.com/nickjbrowning/cuda_mace (2024).
- [93] W. C. Witt, symmetrix, <https://github.com/wcwitt/symmetrix> (2025).
- [94] F. Bigi, G. Fraux, N. J. Browning, and M. Ceriotti, Fast evaluation of spherical harmonics with sphericart, *J. Chem. Phys.*, 064802 (2023).
- [95] Y. Qiu, D. G. Smith, C. D. Stern, M. Feng, H. Jang, and L.-P. Wang, Driving torsion scans with wavefront propagation, *The Journal of chemical physics* **152** (2020).
- [96] D. G. Smith, A. T. Lolinco, Z. L. Glick, J. Lee, A. Ale-naizan, T. A. Barnes, C. H. Borca, R. Di Remigio, D. L. Dotson, S. Ehlert, *et al.*, Quantum chemistry common driver and databases (qcdb) and quantum chemistry engine (qcengine): Automation and interoperability among computational chemistry programs, *The Journal of chemical physics* **155** (2021).
- [97] L.-P. Wang and C. Song, Geometry optimization made simple with translation and rotation coordinates, *The Journal of chemical physics* **144** (2016).
- [98] V. Kapil, J. Wieme, S. Vandenbrande, A. Lemaire, V. Van Speybroeck, and M. Ceriotti, Modeling the structural and thermal properties of loaded metal-organic frameworks. an interplay of quantum and anharmonic fluctuations, *Journal of Chemical Theory and Computation* **15**, 3237–3249 (2019).
- [99] M. Ceriotti, M. Parrinello, T. E. Markland, and D. E. Manolopoulos, Efficient stochastic thermostating of path integral molecular dynamics, *The Journal of Chemical Physics* **133**, 10.1063/1.3489925 (2010).
- [100] V. Kapil, M. Rossi, O. Marsalek, R. Petraglia, Y. Litman, T. Spura, B. Cheng, A. Cuzzocrea, R. H. Meißner, D. M. Wilkins, B. A. Helfrecht, P. Juda, S. P. Bienvenue, W. Fang, J. Kessler, I. Poltavsky, S. Vandenbrande, J. Wieme, C. Corminboeuf, T. D. Kühne, D. E. Manolopoulos, T. E. Markland, J. O. Richardson, A. Tkatchenko, G. A. Tribello, V. Van Speybroeck, and M. Ceriotti, i-pi 2.0: A universal force engine for advanced molecular simulations, *Computer Physics Communications* **236**, 214–223 (2019).
- [101] N. Raimbault, V. Athavale, and M. Rossi, Anharmonic effects in the low-frequency vibrational modes of aspirin and paracetamol crystals, *Physical Review Materials* **3**, 053605 (2019).
- [102] L. Martínez, R. Andrade, E. G. Birgin, and J. M. Martínez, PACKMOL: A package for building initial configurations for molecular dynamics simulations, *Journal of Computational Chemistry* **30**, 2157 (2009).
- [103] P. Eastman, J. Swails, J. D. Chodera, R. T. McGibbon, Y. Zhao, K. A. Beauchamp, L.-P. Wang, A. C. Simmonett, M. P. Harrigan, C. D. Stern, R. P. Wiewiora, B. R. Brooks, and V. S. Pande, OpenMM 7: Rapid development of high performance algorithms for molecular dynamics, *PLOS Computational Biology* **13**, e1005659 (2017).
- [104] M. Brehm and B. Kirchner, TRAVIS - A Free Analyzer and Visualizer for Monte Carlo and Molecular Dynamics Trajectories, *Journal of Chemical Information and Modeling* **51**, 2007 (2011).
- [105] M. Brehm, M. Thomas, S. Gehrke, and B. Kirchner, TRAVIS—A free analyzer for trajectories from molecular simulation, *The Journal of Chemical Physics* **152**, 164105 (2020).
- [106] M. Thomas, M. Brehm, R. Fligg, P. Vöhringer, and B. Kirchner, Computing vibrational spectra from ab initio molecular dynamics, *Physical Chemistry Chemical Physics* **15**, 6608 (2013).
- [107] M. Thomas, M. Brehm, and B. Kirchner, Voronoi dipole moments for the simulation of bulk phase vibrational spectra, *Physical Chemistry Chemical Physics* **17**, 3207 (2015).

V. Supporting Information

A. Training details

Initially, the force weight in the loss was set to 1000 and the energy weight to 40. The learning rate was 0.01 and Adam optimizer with Amsgrad was used. The exponential moving average of the weights was taken in each training step. When the force error converged, the second phase of the training was started with force weight 10 and energy weight 1000 and the learning rate was reduced to 0.00025. Finally, the training was terminated when the energy error also stopped decreasing significantly. All models were trained on a single Nvidia A100 GPU. Training the small model took about 6 days, the medium about 10 days and the large model 14 days.

B. Test set errors

The numerical values of the test set errors are displayed in Table IV. Intermolecular force errors were obtained as RMSEs between DFT intermolecular forces and MACE predictions. The intermolecular forces were computed by summing over the translational and rotational components for each atom as shown in Ref. [65]. The algorithm can be summarized as follows:

1. identify molecules (labeled j)
2. within each molecule j sum over all atomic forces (labeled k) to obtain the translational component:

$$F_j^{\text{trans}} = \sum_{k \in j} f_k \quad (9)$$

3. redistribute the molecular translational force onto individual atoms (labeled i) to obtain the atomic translational contributions:

$$f_i^{\text{trans}} = \frac{m_i}{M_j} F_j^{\text{trans}} \quad (10)$$

where m_i are atomic masses and M_j are molecular masses

4. similarly, compute the torque on the entire molecule:

$$T_j = \sum_{k \in j} f_k \times (r_k - R_j^{\text{com}}) \quad (11)$$

Table IV. Summary of test set errors including inter-molecular force errors

		PubChem	DES370K Monomers	DES370K Dimers	Dipeptides	Solvated Amino Acids	Water	QMugs	Tripeptide	
MAE	E (meV/Å)	23S	1.41	1.04	0.98	0.84	1.60	1.67	1.03	1.05
		23M	0.91	0.63	0.58	0.52	1.21	0.76	0.69	0.57
		23L	0.88	0.59	0.54	0.42	0.98	0.83	0.45	0.38
	F _{total} (meV/Å)	23S	35.68	17.63	16.31	25.07	38.56	28.53	41.45	32.88
		23M	20.57	9.36	9.02	14.27	23.26	15.27	23.58	18.74
		23L	14.75	6.58	6.62	10.19	19.43	13.57	16.93	13.20
	F _{inter} (meV/Å)	23S	0.13	0.18	3.01	0.07	16.98	19.03	0.09	0.07
		23M	0.13	0.18	1.79	0.07	10.30	10.03	0.09	0.07
		23L	0.13	0.18	1.44	0.07	8.85	8.97	0.09	0.07
Relative MAE	E (%)	23S	0.00	0.00	0.00	0.00	0.01	8.44	0.00	0.00
		23M	0.00	0.00	0.00	0.00	0.00	3.84	0.00	0.00
		23L	0.00	0.00	0.00	0.00	0.00	4.18	0.00	0.00
	F _{total} (%)	23S	4.65	2.72	3.46	3.55	3.16	4.50	4.12	3.66
		23M	2.68	1.45	1.91	2.02	1.90	2.41	2.35	2.09
		23L	1.92	1.02	1.40	1.44	1.59	2.14	1.68	1.47
	F _{inter} (%)	23S	nan	nan	15.52	nan	21.66	21.19	nan	nan
		23M	nan	nan	9.25	nan	13.14	11.17	nan	nan
		23L	nan	nan	7.44	nan	11.29	9.99	nan	nan
RMSE	E (meV/Å)	23S	2.74	1.47	1.51	1.26	1.98	2.07	1.28	1.40
		23M	2.02	0.90	0.91	0.85	1.55	0.99	0.89	0.75
		23L	2.48	0.84	0.87	0.70	1.32	0.99	0.58	0.49
	F _{total} (meV/Å)	23S	61.83	26.15	28.48	36.97	53.55	39.33	62.46	71.41
		23M	40.51	14.31	16.81	22.25	32.19	21.40	36.73	33.94
		23L	33.34	10.27	12.81	16.19	26.91	18.78	27.17	22.46
	F _{inter} (meV/Å)	23S	0.78	0.44	8.70	0.13	27.11	27.59	0.17	0.12
		23M	0.79	0.44	5.54	0.13	16.46	15.05	0.17	0.12
		23L	0.76	0.44	4.34	0.13	14.24	13.39	0.17	0.12
Relative RMSE	E (%)	23S	0.00	0.00	0.00	0.00	0.01	8.30	0.00	0.00
		23M	0.00	0.00	0.00	0.00	0.00	3.96	0.00	0.00
		23L	0.00	0.00	0.00	0.00	0.00	3.98	0.00	0.00
	F _{total} (%)	23S	5.56	2.79	4.13	3.63	3.47	4.58	4.66	5.45
		23M	3.64	1.52	2.44	2.19	2.09	2.49	2.74	2.59
		23L	3.00	1.09	1.86	1.59	1.74	2.19	2.03	1.71
	F _{inter} (%)	23S	nan	nan	8.95	nan	20.17	20.18	nan	nan
		23M	nan	nan	5.70	nan	12.25	11.00	nan	nan
		23L	nan	nan	4.46	nan	10.60	9.79	nan	nan

5. compute the rotational atomic force contributions that give rise to the given molecular torque:

$$f_i^{\text{rot}} = m_i (r_i - R_j^{\text{com}}) \times (I_j^{\alpha\beta})^{-1} T_j \quad (12)$$

where $I_j^{\alpha\beta}$ are the molecular moments of inertia

6. compute the vibrational contribution as the difference:

$$f_i^{\text{vib}} = f_i - f_i^{\text{trans}} - f_i^{\text{rot}} \quad (13)$$

7. the intermolecular force is calculated as the sum of the translational and rotational contributions.

Relative errors were obtained by dividing the absolute errors by the typical DFT force magnitudes:

$$\text{Rel MAE} = \frac{\sum_i |f_i^{\text{DFT}} - f_i^{\text{MAE}}|}{\sum_i |f_i^{\text{DFT}} - \bar{f}^{\text{DFT}}|} \quad (14)$$

$$\text{Rel RMSE} = \sqrt{\frac{\sum_i (f_i^{\text{DFT}} - f_i^{\text{MAE}})^2}{\sum_i (f_i^{\text{DFT}} - \bar{f}^{\text{DFT}})^2}} \quad (15)$$

where $\bar{f}^{\text{DFT}} = \sum_i f_i^{\text{DFT}} / N$ is the average DFT force (often zero).

Table IV shows these errors computed for all three MACE models on each category of atomic configurations found in the test set. Interestingly, even though PubChem, DES370K Monomers, Dipeptides, QMugs and Tripeptides comprise only isolated molecule configurations, we find a small error that is incorrectly attributed to intermolecular interactions. This issue arises because DFT forces in these test data do not obey translational and rotational symmetry, i.e. total molecular force and torque do not sum to zero, even though a single molecule is present in each simulation box. Meanwhile, MACE forces do obey these symmetries, and therefore the difference shows up as an intermolecular error which is identical for all three MACE models.

The code used for this analysis is made available on <https://github.com/imagdau/aseMolec.git>.

C. Computational experiment details

1. Torsion angle scanning calculations

The TorsionNet-500 [70] and biaryl torsion [69] benchmark datasets were recomputed at the SPICE [51] level of QM theory (ω B97M-D3(BJ)/def2-TZVPPD [52–56]) to assess the accuracy of the MACE models in predicting the potential energy surfaces of rotatable bonds commonly found in drug-like molecules. Starting from the published optimized geometries, a torsion scan was performed using TorsionDrive [95] via its interface with QCEngine [96]. The dihedral angles were scanned in 15° increments and each constrained geometry optimization was carried out with geomeTRIC [97], using PSI4 [57] to calculate the DFT energies and forces. For each of the assessed force field models, a separate constrained geometry optimization was performed starting from the DFT reference geometries and holding the target torsion fixed at each grid point value. The final RMSD between the optimized and reference geometry was recorded, along with the energy to calculate the potential energy surfaces.

2. Paracetamol crystal spectra

To compute the vibrational spectrum for the paracetamol form II polymorph, we first performed a 20 ps path-integral MD simulation using the MACE-OFF23(S) model at 500 K, following the prescriptions of the Path Integral coarse-Grained Simulations (PIGS) approach [71, 73]. The path-integral MD simulations are performed with a 0.50 fs timestep using the BAOAB integration scheme extended to path-integral MD [98] using the path-integral Langevin equation thermostats [99] with a time constant of 100 fs.

To generate a potential energy surface that effectively encodes quantum nuclear effects, we followed the PIGS technique. We used the positions and forces on the cen-

teroid of the path-integral to fit a MACE model that represents the difference between the potential energy surface and the potential of mean force on the centroid at an elevated temperature of 500 K. The sum of MACE-OFF23(S) and the PIGS model gives a transferable effective potential energy surface that encodes quantum nuclear effects.

To generate a trajectory with quantum nuclear motion, we run MD with the sum of MACE-OFF23(S) and the PIGS model using the *i-PI* [100] software to propagate the equations of motion and the ASE calculator as the force-provider. The MD simulations were performed with a 0.50 fs timestep using a weak global stochastic velocity rescaling thermostat. To generate classical trajectories we perform MD with the same setup but without the PIGS potential.

We predicted the $L = 0$ and $L = 2$ spherical harmonic components of polarizability tensors on the trajectories and computed their time correlation functions to obtain the isotropic and anisotropic Raman spectra [73]. We estimate the powder Raman spectrum as a linear combination of the isotropic and the anisotropic Raman spectra [101].

The model architecture was identical to the MACE architecture used for the energy models, with the only difference being the readout function producing a vector and a tensor (dipole and polarizability) for each atom, instead of the atomic site energies. A relatively small MACE model is already capable of achieving high accuracy predictions, and the selected models used the hyperparameters displayed in Table V.

Table V. Hyperparameters of the MACE models for dipoles and polarizabilities

	Paracetamol Water	
Cutoff radius (Å)	5.0	6.0
Chemical channels	16	32
k (Eq. (1))		
max L (Eq. (5))	2	2

3. Condensed phase simulations

Initial PDB files were taken from Ref. [83] and periodic boxes were generated using packmol [102]. Boxes were prepared containing 64 molecules, with box vectors determined such that the initial density was 80% of the experimental density. Structures were minimised with the L-BFGS algorithm prior to MD. Molecular dynamics was performed with OpenMM, using a custom fork of the `openmm-ml` package to interface MACE models to the MD code.* Simulations were performed in the

* <https://github.com/jharrymoore/openmm-ml/tree/main>

NPT ensemble. The Langevin equations of motion were integrated with a timestep of 1 fs and a Monte Carlo barostat was used to maintain pressure at 1 atm. Temperatures were maintained at 298 K except for those compounds whose boiling point was below this value, for which a value of 10 K below the experimental boiling point was used. Dynamics were propagated for 300 ps, and the final density was calculated by averaging over the final 500 frames of the simulation.

Heat of vaporization calculations additionally required simulation of the isolated molecule in the vacuum phase, which was carried out on a nonperiodic molecule. Final energies for both condensed and vacuum phases were calculated by averaging over the final 500 frames of each trajectory.

The computational details for simulating the classical and quantum dynamical properties of water are the same as the setup for paracetamol (see the previous section).

	MAE	RMSE	r
MACE-OFF23(S)	0.23	0.38	0.20
MACE-OFF23(M)	0.09	0.15	0.89
MACE-OFF24(M)	0.14	0.34	0.26
ANI-2x	0.21	0.36	0.26

Table VI. **Summary of density errors**

	MAE	RMSE	r
MACE-OFF23(S)	1.48	2.19	0.86
MACE-OFF23(M)	2.18	2.53	0.87
MACE-OFF24(M)	1.75	2.81	0.78
ANI-2x	2.75	3.45	0.66

Table VII. **Summary of ΔH_{vap} errors**

4. *Ala₃ Free Energy Surface*

Molecular dynamics simulations were performed with OpenMM, as in the previous section. Enhanced sampling simulations were performed with metadynamics. Two collective variables were defined by the two torsion angles on the backbone of the central alanine residue. A 1 ns simulation was performed with a temperature bias factor of 10, a barrier height of 1 kJ/mol and a frequency of 100 steps.

5. *Crambin in explicit solvent*

Crambin was prepared from the PDB structure 1EJG. The initial structure was prepared using pdbfixer [103] and solvated in an orthorhombic box with padding between solute and the box edge set to 1.2 nm.

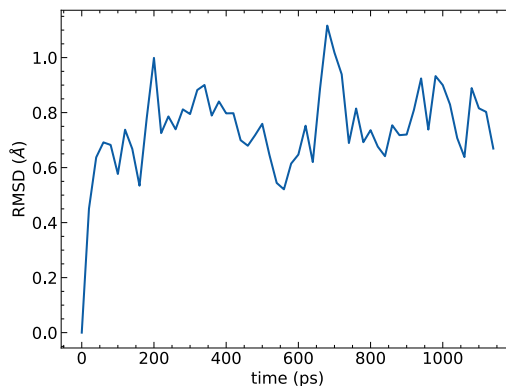


Figure 17. **Crambin RMSD.** RMSD calculated by averaging two halves of a 1 ns trajectory, relative to the first frame and computed on C_{α} atoms.

Dynamics were performed in the NPT ensemble, with pressure maintained at 1 atm with a Monte Carlo barostat, as implemented in OpenMM. A 1 fs timestep was used both for integrating the Langevin equations of motion and for writing the trajectory to disk for post processing. The power spectrum was calculated as the Fourier transform of the velocity autocorrelation function using the Travis program with default settings [104–107].

D. **Lattice enthalpies**

First, the internal energy of the crystalline form was computed under the harmonic approximation:

$$\begin{aligned}
 U(T) &= \left(\frac{\partial \ln Z}{\partial \frac{1}{k_B T}} \right) \\
 &= E_{\text{MACE}} + \int_0^{\infty} \left[\frac{\epsilon}{e^{\frac{\epsilon}{k_B T}} - 1} + \frac{\epsilon}{2} \right] \sigma(\epsilon) d\epsilon
 \end{aligned} \tag{16}$$

where Z denotes the partition function of the system, and $\sigma(\epsilon)$ represents the degeneracy or phonon density of states as a function of vibrational energy. The above expression contains an electronic contribution, computed using MACE, a zero point energy contribution, and a contribution from finite-temperature vibrational energy. To compute the vibrational contribution, we used a $3 \times 3 \times 3$ supercell for all the molecules considered. For the gaseous form of the molecules, we employed the ideal gas approximation to compute the enthalpies of the gas as:

$$U(T) = e_{\text{MACE}} + E_{\text{ZPE}} + \int_0^T C_p dT \tag{17}$$

where we used the ideal gas value to evaluate the last term, giving $4RT$ for all system except for the linear carbon-dioxide, where the value is $3.5RT$.

Combining the above two expressions, we can compute the sublimation enthalpies as:

$$\begin{aligned}\Delta H_{\text{subm}} &= U_{\text{gas}}(T) - U_{\text{cryst}}(T) \\ &= E_{\text{latt}} + \Delta E_{\text{vib}} + 4RT\end{aligned}\quad (18)$$

To assess the accuracy of the MACE model we used the X23 set of molecular crystals [78]. We first relaxed the cells, followed by phonon and normal mode calculations to obtain the finite temperature vibrational as well as zero point contributions to the enthalpies, following the protocol above. It is important to note that for the ANI-2x force field it was not possible to fully relax the crystal geometries, because the model cannot predict stresses. Hence, we kept the cell fixed at the DFT equilibrium values from Ref. [78]. The results are summarized in Table VIII.

Table VIII. **Sublimation enthalpy in kJ/mol**

System	ΔH_{sub}^0 exp.	ΔH_{sub}^0 MACE-OFF23(L)	ΔH_{sub}^0 ANI-2x
1,4-Cyclohexanedione	81.1	85.1	59.7
Acetic acid	67.7	70.3	90.7
Adamantane	61.6	69.2	67.1
Ammonia	31.2	26.8	23.0
Anthracene	101.9	106.3	98.9
Benzene	44.9	58.4	48.3
Carbon dioxide	26.1	4.1	-117.9
Cyanamide	75.5	87.3	36.9
Cytosine	156.4	143.2	118.6
Ethyl carbamate	78.8	91.4	77.0
Formamide	71.7	80.1	67.3
Hexamine	75.8	62.3	83.5
Imidazole	81.4	86.3	86.6
Naphthalene	72.6	83.6	72.4
Oxalic acid α	93.7	89.7	44.1
Oxalic acid β	93.6	93.5	45.4
Pyrazine	56.3	69.7	53.7
Pyrazole	72.4	73.0	75.4
s-Triazine	55.7	75.6	112.1
s-Trioxane	56.3	53.9	51.7
Succinic acid	123.1	123.5	141.7
Uracil	129.2	131.8	98.9
Urea	93.8	112.5	78.2

E. Crystal structure geometries

In Table IX we compare the MACE-OFF23(L) relaxed crystal structure lattice parameters with the experimental ones reported in Ref. [79]. We confirm that MACE is able to accurately reproduce the lattice constant of molecular crystals purely trained on molecular dimers. Additional trimer training data, or a higher level of reference theory, such as coupled cluster, could probably further improve the agreement with experiments.

Table IX. **Crystal structure geometries**

Molecule	T_{exp}	Experiment	MACE-OFF23(L)
Acetic acid	40	<i>a</i>	13.151
		<i>b</i>	3.923
		<i>c</i>	5.762
		<i>V</i>	297.27
Ammonia	2	<i>a</i>	5.048
		<i>V</i>	128.63
Benzene	4	<i>a</i>	7.351
		<i>b</i>	9.364
		<i>c</i>	6.695
		<i>V</i>	460.84
Naphthalene	10	<i>a</i>	8.0846
		<i>b</i>	5.9375
		<i>c</i>	8.6335
		β	124.67
		<i>V</i>	340.83
Pyrazine	184	<i>a</i>	9.325
		<i>b</i>	5.850
		<i>c</i>	3.733
		<i>V</i>	203.64
Urea	40	<i>a</i>	5.565
		<i>c</i>	4.684
		<i>V</i>	145.06